10-3-2018

Compromised Phagosome Maturation Underlies RPE Pathology in Cell Culture and Whole Animal Models of Smith-Lemli-Opitz Syndrome

Sriganesh Ramachandra Rao

Bruce A. Pfeffer

Néstor Más Gómez
University of Pennsylvania

Lara A. Skelton

Ueda Keiko

See next page for additional authors

Recommended Citation

Ramachandra Rao, S., Pfeffer, B. A., Más Gómez, N., Skelton, L. A., Keiko, U., Sparrow, J. R., Rowsam, A. M., Mitchell, C. H., & Fliesler, S. J. (2018). Compromised Phagosome Maturation Underlies RPE Pathology in Cell Culture and Whole Animal Models of Smith-Lemli-Opitz Syndrome. *Autophagy, 14* (10), 1796-1817. http://dx.doi.org/10.1080/15548627.2018.1490851

Compromised Phagosome Maturation Underlies RPE Pathology in Cell Culture and Whole Animal Models of Smith-Lemli-Opitz Syndrome

Abstract

Treatment of rats with the cholesterol pathway inhibitor AY9944 produces an animal model of Smith-Lemli-Opitz syndrome (SLOS), an autosomal recessive disease caused by defective cholesterol synthesis. This SLOS rat model undergoes progressive and irreversible degeneration of the neural retina, with associated pathological features of the retinal pigmented epithelium (RPE). Here, we provide further insights into the mechanism involved in the RPE pathology. In the SLOS rat model, markedly increased RPE apical autofluorescence is observed, compared to untreated animals, which correlates with increased levels of A2E and other bisretinoids. Utilizing cultured human induced pluripotent stem cell (iPSC)- derived SLOS RPE cells, we found significantly elevated steady-state levels of 7-dehydrocholesterol (7DHC) and decreased cholesterol levels (key biochemical hallmarks of SLOS). Western blot analysis revealed altered levels of the macroautophagy/autophagy markers MAP1LC3B-II and SQSTM1/p62, and build-up of ubiquitinated proteins. Accumulation of immature autophagosomes was accompanied by inefficient degradation of phagocytized, exogenously supplied retinal rod outer segments (as evidenced by persistence of the C-terminal 1D4 epitope of RHO [rhodopsin]) in SLOS RPE compared to iPSC-derived normal human control. SLOS RPE cells exhibited lysosomal pH levels and CTSD activity within normal physiological limits, thus discounting the involvement of perturbed lysosomal function. Furthermore, 1D4-positive phagosomes that accumulated in the RPE in both pharmacological and genetic rodent models of SLOS failed to fuse with lysosomes. Taken together, these observations suggest that defective phagosome maturation underlies the observed RPE pathology. The potential relevance of these findings to SLOS and the requirement of cholesterol for phagosome maturation are discussed. © 2018, © 2018 Informa UK Limited, trading as Taylor & Francis Group.

Keywords

Autophagy, cholesterol, lysosomes, phagosome maturation, RPE, Smith-Lemli-Opitz, Animals, Biomarkers, Cathepsin D, Cattle, Cell Culture Techniques, Dehydrocholesterols, Disease Models, Animal, Humans, Lysosomes, Membrane Fusion, Phagocytosis, Phagosomes, Protein Biosynthesis, Rats, Retinal Pigment Epithelium, Retinoids, Rod Cell Outer Segment, Smith-Lemli-Opitz Syndrome, trans-1, 4-Bis(2-chlorobenzaminomethyl)cyclohexane Dihydrochloride, Transcription, Genetic, Ubiquitinated Proteins, 7 dehydrocholesterol, microtubule associated protein 1, microtubule associated protein 1 light chain 3beta, rhodopsin, sequestosome 1, ubiquitinated protein, unclassified drug, 1, 4 bis(2 chlorobenzylaminomethyl)cyclohexane, 7 dehydrocholesterol, 7-dehydrocholesterol, biological marker, cathepsin D, retinoid, ubiquitinated protein, animal experiment, animal model, Article, autofluorescence, autophagosome, cell level, cell maturation, cholesterol level, controlled study, degradation, human, human cell, induced pluripotent stem cell, lysosome, nonhuman, phagocytosis, phagosome, rat, retinal pigment epithelium, retinal rod outer segment, Smith Lemli Opitz syndrome, stem cell culture, Western blotting, animal, bovine, cell culture technique, disease model, genetic transcription, genetics, membrane fusion, metabolism, pathology, phagosome, protein synthesis, retinal pigment epithelium, Smith Lemli Opitz syndrome

Disciplines

Dentistry

Author(s)

Sriganesh Ramachandra Rao, Bruce A. Pfeffer, Néstor Más Gómez, Lara A. Skelton, Ueda Keiko, Janet R. Sparrow, Aryn M. Rowsam, Claire H. Mitchell, and Steven J. Fliesler

Autophagy

Autophagy

ISSN: 1554-8627 (Print) 1554-8635 (Online) Journal homepage: https://www.tandfonline.com/loi/kaup20

Compromised phagosome maturation underlies RPE pathology in cell culture and whole animal models of Smith-Lemli-Opitz Syndrome

Sriganesh Ramachandra Rao, Bruce A. Pfeffer, Néstor Más Gómez, Lara A. Skelton, Ueda Keiko, Janet R. Sparrow, Aryn M. Rowsam, Claire H. Mitchell & Steven J. Fliesler

To cite this article: Sriganesh Ramachandra Rao, Bruce A. Pfeffer, Néstor Más Gómez, Lara A. Skelton, Ueda Keiko, Janet R. Sparrow, Aryn M. Rowsam, Claire H. Mitchell & Steven J. Fliesler (2018) Compromised phagosome maturation underlies RPE pathology in cell culture and whole animal models of Smith-Lemli-Opitz Syndrome, Autophagy, 14:10, 1796-1817, DOI: 10.1080/15548627.2018.1490851

To link to this article: https://doi.org/10.1080/15548627.2018.1490851

AUTOPHAGY
2018, VOL. 14, NO. 10, 1796–1817
https://doi.org/10.1080/15548627.2018.1490851

Taylor & Francis
Taylor & Francis Group

RESEARCH PAPER - BASIC SCIENCE

Compromised phagosome maturation underlies RPE pathology in cell culture and whole animal models of Smith-Lemli-Opitz Syndrome

Sriganesh Ramachandra Rao[a,b,c], Bruce A. Pfeffer[a,b,c], Néstor Más Gómez[d], Lara A. Skelton[a,b,c], Ueda Keiko[e], Janet R. Sparrow[e], Aryn M. Rowsam[a,b,c], Claire H. Mitchell[d], and Steven J. Fliesler[a,b,c]

[a]Departments of Ophthalmology (Ross Eye Institute) and Biochemistry, Jacobs School of Medicine and Biomedical Sciences, SUNY-University at Buffalo, Buffalo, NY, USA; [b]SUNY Eye Institute, Buffalo, NY, USA; [c]Research Service, VA Western NY Healthcare System, Buffalo, NY, USA; [d]Department of Anatomy & Cell Biology, University of Pennsylvania, School of Dental Medicine, Philadelphia, PA, USA; [e]Departments of Ophthalmology (Harkness Eye Institute) and Pathology & Cell Biology, Columbia University, College of Physicians & Surgeons, NY, NY, USA

ABSTRACT

Treatment of rats with the cholesterol pathway inhibitor AY9944 produces an animal model of Smith-Lemli-Opitz syndrome (SLOS), an autosomal recessive disease caused by defective cholesterol synthesis. This SLOS rat model undergoes progressive and irreversible degeneration of the neural retina, with associated pathological features of the retinal pigmented epithelium (RPE). Here, we provide further insights into the mechanism involved in the RPE pathology. In the SLOS rat model, markedly increased RPE apical autofluorescence is observed, compared to untreated animals, which correlates with increased levels of A2E and other bisretinoids. Utilizing cultured human induced pluripotent stem cell (iPSC)- derived SLOS RPE cells, we found significantly elevated steady-state levels of 7-dehydrocholesterol (7DHC) and decreased cholesterol levels (key biochemical hallmarks of SLOS). Western blot analysis revealed altered levels of the macroautophagy/autophagy markers MAP1LC3B-II and SQSTM1/p62, and build-up of ubiquitinated proteins. Accumulation of immature autophagosomes was accompanied by inefficient degradation of phagocytized, exogenously supplied retinal rod outer segments (as evidenced by persistence of the C-terminal 1D4 epitope of RHO [rhodopsin]) in SLOS RPE compared to iPSC-derived normal human control. SLOS RPE cells exhibited lysosomal pH levels and CTSD activity within normal physiological limits, thus discounting the involvement of perturbed lysosomal function. Furthermore, 1D4-positive phagosomes that accumulated in the RPE in both pharmacological and genetic rodent models of SLOS failed to fuse with lysosomes. Taken together, these observations suggest that defective phagosome maturation underlies the observed RPE pathology. The potential relevance of these findings to SLOS and the requirement of cholesterol for phagosome maturation are discussed.

ARTICLE HISTORY
Received 10 August 2017
Revised 25 May 2018
Accepted 11 June 2018

KEYWORDS
Autophagy; cholesterol; lysosomes; phagosome maturation; RPE; Smith-Lemli-Opitz

Introduction

Smith-Lemli-Opitz Syndrome (SLOS) (OMIM: 270,400) is the most common recessive genetic disorder of the cholesterol biosynthetic pathway (frequency 1:20,000–1:60,000 live births, and carrier frequency of 1:30), caused by mutations in the gene coding for 7-dehydrocholesterol reductase (3β-hydroxysterol-Δ^7-reductase, *DHCR7*) [1]. DHCR7 catalyzes the last step of cholesterol synthesis, the NADPH-dependent reduction of the Δ^7 bond of 7-dehydrocholesterol (7DHC) to form cholesterol (Chol) [2]. Over 150 mutations in the human *DHCR7* gene have been reported (reviewed in [3]), causing reduced steady-state levels of Chol and increased levels of 7DHC and 7DHC-specific oxysterols in plasma and all bodily tissues of affected individuals [4–8]. Although no strict genotype-phenotype correlations exist, common SLOS phenotypic manifestations include mental retardation, autism, and a variety of dysmorphologies, particularly 2,3-toe syndactyly, craniofacial malformations, cardiovascular malformations and skeletal defects, as well as visual deficits and vision-associated electrophysiological abnormalities [1,9–12]. An electroretinographic (ERG) study on a cohort of 13 SLOS patients indicated significantly attenuated rod photosensitivity involving slow activation and deactivation kinetics of the phototransduction cascade [12]. We have previously reported the biochemical (lipidomic and proteomic), histological, ultrastructural, electroretinographic and cell-death characteristics of a time-dependent retinal degeneration that occurs in a pharmacologically-induced rat model of SLOS, produced by treatment of normal Sprague-Dawley rats with AY9944 (*trans*-1,4-bis[2-chlorobenzylaminoethyl] cyclohexane dihydrochloride), a relatively specific inhibitor of DHCR7 [13–17]. Dramatic alterations are observed in the sterol composition of all tissues examined (including blood, liver, retina, and brain), with 7DHC:Chol mole ratios > 5 (this ratio is typically < 0.01 under normal conditions) [13]. Electron microscopy analysis of the retina and retinal pigment epithelium (RPE) in this model reveals defects in the ability of the RPE to efficiently degrade and eliminate phagocytized retinal rod outer segment (OS) material, even prior to onset of obvious

CONTACT Steven J. Fliesler fliesler@buffalo.edu Research Service, Buffalo VA Medical Center/VAWNYHS, 3495 Bailey Avenue- Mail Stop 151, Buffalo, NY, 14215-1129, USA

Supplemental data can be accessed here.

degenerative features in the neural retina (at postnatal day 30 [P30]) [13], and the continued OS accumulation is observed at P80 [18]. The RPE in AY9944-treated rats exhibits excessive accumulation of phagosomes, lipid-rich particles and other cytoplasmic inclusions, indicative of compromised organelle clearance. Apart from basal damaged intracellular organelle clearance (autophagy), the lysosome-dependent degradation process of the OS disks in the RPE is indispensable for OS homeostasis (heterophagy), and thereby for maintaining normal visual function (reviewed in [19]). Hence, we have revisited this SLOS animal model with a focus on the pathological features of the RPE and the mechanism(s) by which they arise. We propose that defective clearance of accumulated material in the RPE contributes to the observed retinal degeneration, and is due to deranged Chol synthesis plus the formation and build-up of cytotoxic 7DHC-derived oxysterols.

The RPE consists of a single layer of post-mitotic, polarized, cuboidal epithelial cells sandwiched between the neural retina and the choroidal blood supply, and forms the outer blood-retinal barrier. Major functions of the RPE include nutrient transport to, and waste transport away from, photoreceptors; replenishment of the 11-*cis*-retinaldehyde chromophore necessary to regenerate the visual pigment rhodopsin (via action of the 'visual cycle'); and diurnal heterophagic degradation of the shed tips of the photoreceptor (rod and cone) OS (reviewed in [19,20]). In mammals, retinal rod photoreceptors shed about 10% of their apical OS material daily; the shed OS tips are then phagocytically degraded by the RPE ('heterophagy'), using, in part, the same phagolysosomal machinery that degrades endogenous intracellular material, such as damaged organelles ('autophagy') [21]. A single RPE cell may be responsible for processing the shed OS membranes from up to 50 photoreceptor cells; hence, the phagocytic processing burden of the RPE is substantial, especially when considered over the lifetime of the organism. Direct interference with this clearance pathway, either at the level of phagocytic uptake, or phagosome maturation, or lysosomal function, leads to retinopathies. For example, chloroquine (CHQ)-induced maculopathy [22–25]: CHQ is a quaternary amine, which can alkalinize lysosomal pH, thereby compromising lysosomal function. Similarly, rodent mutant and knockout models of key players of phagocytic uptake, and the autophagic machinery, such as *Mertk* and *Atg5*, exhibit altered phagocytosis and deficient OS degradation accompanied by defective rod photosensitivity, respectively [26,27]. Three observations (in chronological order) of the degenerating retina in the AY9944-induced SLOS rat model are: 1) altered OS processing by the RPE starting around the third postnatal week, followed by 2) progressive shortening of photoreceptor OS length, and 3) photoreceptor-specific cell death, which continues thereafter to about 3 months (the longest time point studied) [13].

In the present study, we investigated the mechanism(s) underlying the clearance defect in the RPE previously documented using the AY9944-induced SLOS rat model, with the ultimate goal of understanding more fully the mechanism(s) underlying the observed retinal degeneration in that model, and their correlations to the human disease. Given that investigation of dynamic cellular processes in complex metabolic diseases such as SLOS can be challenging, we employed a combination of *in vivo* (whole organisms) as well as *in vitro* (cell culture) models that mimic key hallmarks of the disease.

Results

Characterization of control and SLOS RPE cells

To facilitate investigation of the mechanism underlying RPE pathology observed *in vivo* in the SLOS rat model, we set out to generate a convenient, reliable, and clinically relevant *in vitro* model (see *Discussion* for rationale). RPE cells were generated from iPSCs that had been reprogrammed from skin fibroblasts of clinically diagnosed and well-characterized SLOS patients [28]. We first characterized the morphological, biochemical, and genotypic parameters of this novel RPE *in vitro* model. These features were compared with control RPE cells – in this case, iPSC-derived normal, control RPE cells reprogrammed from skin fibroblasts obtained from a normal neonatal human subject (ATCC-Dys0100), or RPE cells reprogrammed from human embryonic stem cells (HsESCs) that were obtained from a human donor lacking any currently known disease-associated mutations.

Epithelial morphology was recorded by bright-field, phase-contrast and immunofluorescence microscopy. As shown in Figure 1, cultures of both control iPSC-derived RPE cells (control RPE) (Figure 1a) and SLOS iPSC-derived RPE cells (SLOS RPE) (Figure 1b) exhibit melanin-containing, confluent monolayers with phase-bright cellular borders (Figure 1(c,d)). Polarized control and SLOS RPE cells also routinely formed 'domes' (representative dome: white asterisk, Figure 1d), *i.e.*, patches of the cellular monolayer that bulged up from the culture substrate, an expected result of vectorial (apical to basolateral) transport of ions and water (not shown) [29]. We observed TJP1 (tight junction protein 1)-positive cell borders (*green* channel) and RLBP1 (retinaldehyde binding protein 1; *red* channel) cytoplasmic immunoreactivity in both control RPE (Figure 1e) and SLOS RPE (Figure 1f) cell cultures. The TJP1-positive cell border of SLOS RPE (Figure 1f) appears aberrant, along with unexpected cytoplasmic punctate staining (white arrows, Figure 1f). To test if the pathologic appearance of SLOS RPE affects transepithelial electrical resistance (TEER), we maintained control and SLOS RPE cells on laminin-coated Transwell® inserts, and performed weekly measurements of TEER (after subtracting TEER measured from plain inserts). Surprisingly, the SLOS RPE cells established healthy monolayers (as we have observed serially), with robust TEER (> 300 $\Omega^{*}cm^{2}$) within 2 to 3 weeks, earlier than control cells (Figure 1g).

Western blot analysis (Figure 1h), using passage 6 control and SLOS RPE cells, showed expression of known RPE markers: RLBP1 (a key player in the visual cycle [30]), acetylated TUBA/α-tubulin (a marker for RPE cilia, and generally required for phagosome maturation [31,32]), BEST1/bestrophin-1, a basolaterally located chloride channel [33]), and KRT8 (keratin 8)-KRT18. In addition, qPCR analysis (Figure 1i) revealed significant (*ca.* 10^{3}- to 10^{5}-fold) enrichment of RPE-specific transcripts, including *RPE65*,

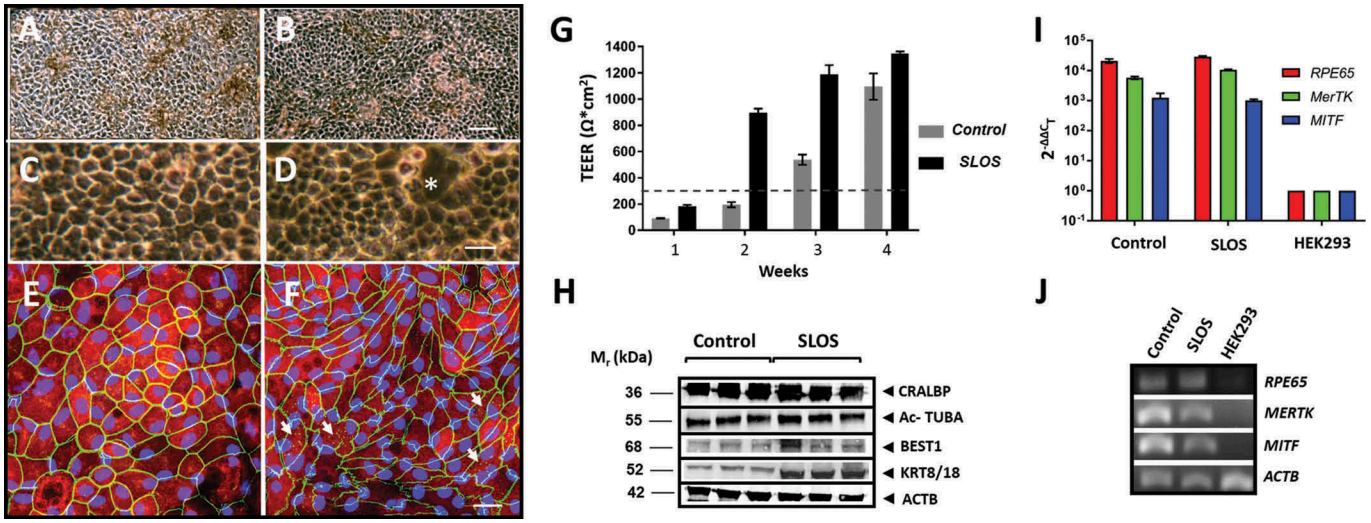

Figure 1. Both control and SLOS RPE cells exhibit morphological, transcriptional, translational and functional features of RPE. Phase-contrast microscopy images of cultured control (**a,c**) and SLOS (**b,d**) RPE cells exhibit establishment of stable monolayers having the characteristic morphological features of RPE cells, including polygonal shape, phase-bright borders, and a 'cobblestone'-like appearance. Dark pigmentation indicates the presence of melanin, another key feature of RPE cells. Higher magnification confocal fluorescence microscopy images of control (**e**) and SLOS (**f**) RPE cells demonstrate expression of characteristic RPE markers, including TJP1-positive tight junctions (green) and cellular RLBP1 (red). DAPI nuclear stain is shown in blue. Scale bars: (**a,b**) 40 μm; (**c,d**) 20 μm; (**e,f**) 5 μm. Please observe aqueous domes (white asterisk, panel **d**), a signature of polarized RPE cultured on non-permeable membrane. Although SLOS RPE cells exhibit cytoplasmic TJP1 labeling (white arrows, panel **f**), and occasionally aberrant cell borders decorated with TJP1, both control and SLOS RPE cells exhibit robust transepithelial electrical resistance (TEER) values (> 300 Ω*cm^2, denoted by gray dotted line, panel **g**). Correlative western blot analysis (**h**) shows that both control and SLOS RPE cells express functional RPE markers: RLBP1, acetylated TUBA/α-tubulin, BEST1, and KRT8-KRT18; ACTB was used as a loading control. (**i**) qPCR analysis demonstrated expression of RPE marker transcripts: *RPE65, MERTK*, and *MITF*. (**j**) Corresponding agarose gel electrophoresis image of qPCR products.

MERTK, and *MITF*, in control and SLOS RPE (normalized to *ACTB* mRNA), relative to expression levels in HEK293S cells (which served as a negative control [34]), further validating our strategy of cell culture and propagation [35,36]. [Note the log scale of the Y-axis, Figure 1i.] The data represent normalized expression ratios for the RPE-specific transcripts from control and SLOS RPE cells, in comparison to HEK293S cells. The corresponding gel image of the PCR products is shown in Figure 1j. Preliminary RNA-Seq analysis of iPSC-derived control and SLOS RPE cells (S.J. Fliesler and M.H. Farkas, unpublished) also suggests that both lines of RPE cultures express > 90% of known RPE-specific transcripts, thus reinforcing confidence in those RPE cell cultures as suitable *in vitro* models.

A commonly occurring SLOS point mutation is the T93M point mutation of DHCR7, resulting in a mild, hypomorphic enzymatic defect [3]. IVS8-1G> C is the most common SLOS mutation, occurring at the junction of intron 8 and exon 9; thus, inhibits splicing of intron 8 in the mRNA. This mutation causes 'nonsense' translation of the predicted NADPH binding domain of DHCR7, producing a nonfunctional enzyme [37]. The original 'CWI' donor fibroblasts utilized to generate SLOS RPE harbored compound heterozygous mutations (T93M and IVS8-1G> C) (based upon the genotype information previously determined from the patient-derived fibroblasts and the iPSCs derived therefrom (refs [28,38]. and F.D. Porter, personal communication). The PCR assay for T93M and IVS8-1G> C mutations yielded gene products of 296 bp and 557 bp (see Fig. S1A). The PCR product was sequenced and the sequencing outputs were aligned against the published *DHCR7* sequence (NM_001360). Sequence alignment (see Fig. S1B) confirmed the occurrence of the expected compound heterozygous mutation in the SLOS RPE cells.

Increase in steady-state levels of 7DHC and ubiquitinated protein load in SLOS RPE cells

Since SLOS RPE cells harbor verified mutant *DHCR7* alleles, they would be expected to show an increase in *de novo* cellular 7DHC levels and the 7DHC:Chol mole ratio, compared to those values obtained with normal (nhRPE) cells. To test this, we performed reverse-phase HPLC analysis on the nonsaponifiable lipids extracted from both HsESC-derived nhRPE and SLOS RPE cells that had been maintained in culture medium supplemented with 0.9% delipidated (*i.e.*, sterol-depleted) bovine calf serum (BCS) for 2 weeks (after culturing in high-calcium medium with 0.9% neat BCS for 2 months). [The rationale for this approach is provided in the *Discussion*.] We empirically determined that the protocol used for delipidation of serum removed *ca.* 99% of the sterols (see Fig. S2A). The cellular sterol composition observed under the culture conditions employed is representative of steady-state levels of the *de novo* synthesized sterol pool. We found that the 7DHC:Chol mole ratio for SLOS RPE was 0.697 ± 0.064 (n = 3), which was ~ 20-fold greater ($P < 0.01$, Welch t test) than that of nhRPE (0.035 ± 0.009; n = 3) (see Fig. S2A for graphical representation; and Fig. S2B, which shows representative HPLC chromatograms from which the quantitative data were derived). We assume that the residual 7DHC observed in nhRPE is a

reflection of the Chol synthesis pathway in flux under the culture conditions employed. Regardless, the highly elevated 7DHC:Chol mole ratio observed in SLOS RPE cells is indicative of hampered DHCR7 catalytic activity, consistent with the verified *DHCR7* mutations in those cells and the original donor source.

The heterophagic pathway in the RPE of the SLOS rat model is compromised (as evidenced in [13,18]). Several lines of evidence implicate autophagy in the clearance of ubiquitinated protein load [39,40]. Further, the mevalonate pathway regulates proteostasis through autophagy [41,42]. To test whether proteostasis was occurring in SLOS RPE, we performed immunoblot analysis of control and SLOS RPE cells, probing the blots with anti-ubiquitin antibody. As shown in Figure 2(b,c), SLOS RPE cells exhibited increased steady-state levels of ubiquitinated proteins, relative to control RPE cells.

Lysosomal ph and CTSD activity of SLOS RPE is within normal physiological range

One possible explanation for the proposed RPE phagolysosomal processing defect in the SLOS rat model might be defective lysosomal function. Experimentally, this dysfunction can be induced in normal cells by treatment with lysosomal alkalinizing agents (*e.g.*, quaternary amines, such as CHQ or NH_4Cl). The lysosomal lumen is normally acidic (pH ~ 4.5), corresponding to the pH optima of various lysosomal proteases, including CTSD (cathepsin D). Experimental approaches to facilitate the understanding of lysosomal function in the context of health and disease have been established and successfully applied using various *in vitro* models [43,44]. Here, we directly measured lysosomal pH with a pH-sensitive dye, and also employed a BODIPY-tagged pepstatin-A-based binding assay (see *Methods*, below) as a surrogate for estimating CTSD activity to assess lysosomal function in SLOS RPE *vs.* control RPE cells in culture.

Lysosomal pH was measured in SLOS RPE cells cultured in medium containing either 0.9% normal BCS or delipidated BCS (DLS). The ability of the assay to detect a broad pH range (pH 4.0–6.0) was validated by our calibration data (see representative calibration, Fig. S3). The difference in mean lysosomal pH values measured in SLOS RPE cells cultured in 0.9% BCS (pH 4.50 ± 0.02) *vs.* SLOS RPE cells cultured in 0.9% DLS (pH 4.65 ± 0.03) was statistically significant ($P < 0.05$, n = 15 each), although both means were within the normal range for lysosomes and the pH optima range for lysosomal enzymes (Figure 3a). CTSD activity (Figure 3b) mirrored the trends observed in lysosomal pH values under both culture conditions. CTSD activity values (expressed as Relative Fluorescence Units, RFU) in SLOS RPE cells cultured in 0.9% BCS were significantly higher ($P < 0.05$), relative to the values obtained from cells cultured in normal 0.9% DLS. Therefore, lysosomal function in SLOS RPE cells may not be optimal when cultured in the presence of delipidated serum. Since we cannot rule out the possibility of a role of altered lysosomal pH in phagosome clearance when cultured in delipidated serum, the next set of autophagy and heterophagy-related experiments were performed in the presence of 0.9% BCS (containing Chol), comparing iPSC-derived control and SLOS RPE cells in parallel.

Alterations in autophagic markers, phagosome maturation, and rod outer segment clearance in SLOS RPE cells

The autophagy process can be monitored using well-defined protein markers such as MAP1LC3B-II/LC3B-II (microtubule associated protein 1 light chain 3 beta) and SQSTM1 [45]. LC3B-II is a lipidated (conjugated with phosphatidylethanolamine) derivative of LC3B-I, a cytosolic protein; lipidation anchors the protein to associate with the phagophore membrane, and its level correlates with autophagosomal volume [46]. The SQSTM1 protein binds to ubiquitinated cargo, interacts with LC3B-II, and is subsequently degraded through autophagy [47]; hence, SQSTM1 serves as a faithful proxy for assessing autophagic processing. However, the steady-state level of either protein, although potentially informative, does

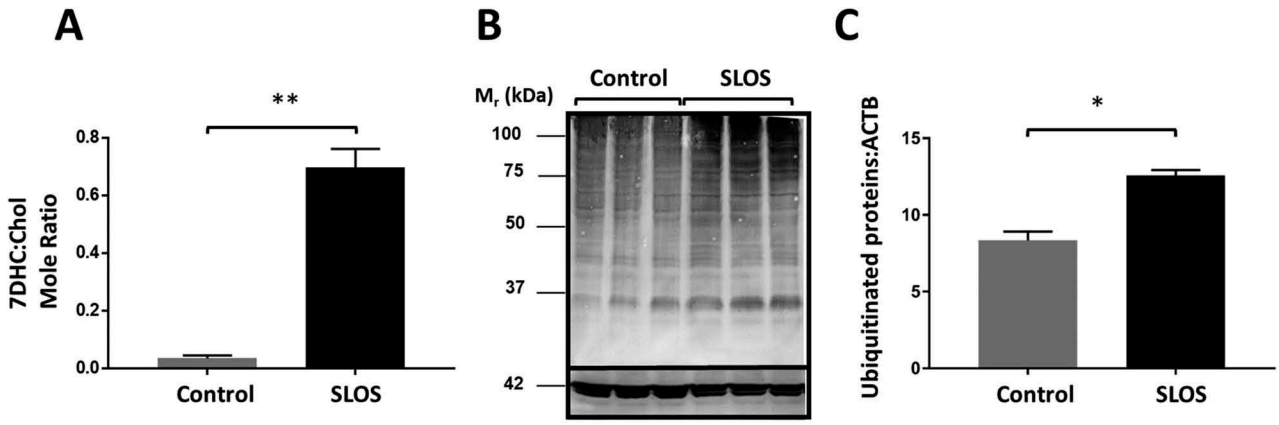

Figure 2. Elevated 7DHC steady-state level is accompanied by ubiquitinated protein accumulation in SLOS RPE cells. 7DHC and Chol levels were measured in both normal human (nhRPE; control) and SLOS RPE cells using reverse phase-HPLC (see Fig. S2B). **(a)** Graphical representation of 7DHC:Chol mole ratio, demonstrating markedly and statistically elevated 7DHC steady-state level in SLOS *vs.* control RPE cells. (**b**) Western blot analysis of control and SLOS RPE cells, probing with anti-ubiquitin antibody, and (**c**) corresponding densitometric quantification, illustrating a ~ 1.5-fold increase in steady-state levels of ubiquitinated proteins in SLOS *vs.* control RPE cells. *$P < 0.05$, ** $P < 0.01$, Welch (unpaired) t test.

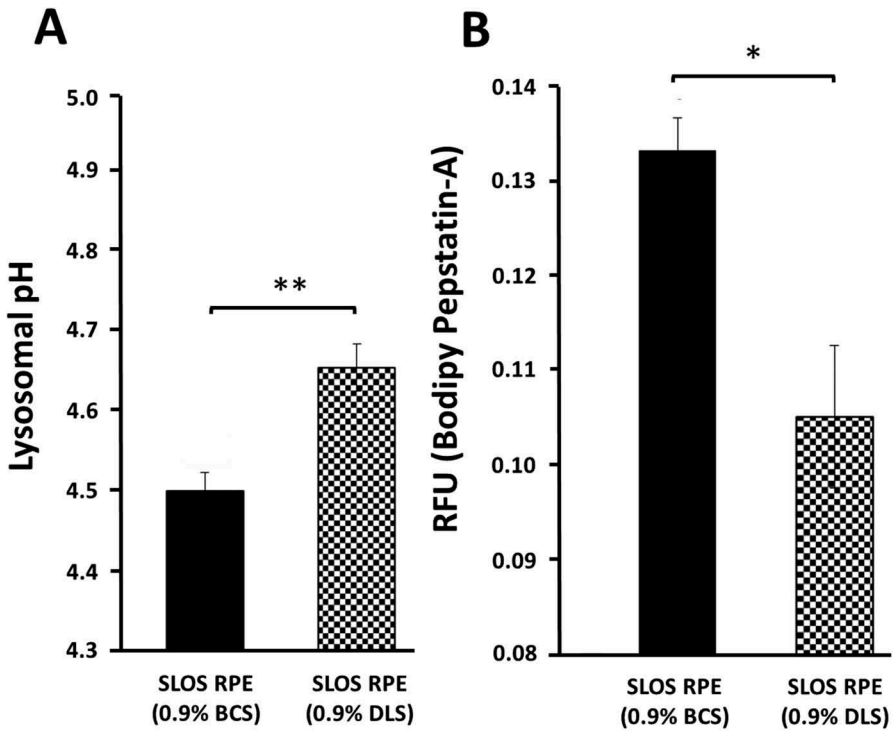

Figure 3. Lysosomal pH and CTSD activity in SLOS RPE cells is within normal physiological range. (**a**) Graphical representation of lysosomal pH values of SLOS RPE cells supplied with normal *vs*. delipidated serum (n = 15 each). When cultured in medium containing 0.9% (v:v) unprocessed BCS, lysosomal pH in SLOS RPE cells was within the normal physiological range (pH 4.5). Lysosomal pH of SLOS RPE was slightly alkalinized (by *ca*. 0.15 pH units, $^{**}P < 0.01$) when cultured in medium containing 0.9% (v:v) delipidated serum (DLS; where > 90% of sterol had been removed). (**b**) Graphical representation of CTSD activity of SLOS RPE cells incubated in medium containing standard (BCS) and delipidated serum (DLS) (n = 15 each). CTSD activity was lower when the culture medium contained 0.9% DLS as compared to 0.9% BCS, in agreement with lysosomal pH measurements, corresponding to mild acidification of lysosomes in cells cultured in 0.9% DLS, indicating a deviation from optimal pH for this lysosomal enzyme activity. $^{*}P < 0.05$, $^{**}P < 0.01$; Welch (unpaired) t test.

not directly reflect autophagic flux [48,49]. To investigate autophagic flux, we treated both SLOS RPE and control RPE cells with a physiologically perturbing, but tolerated, concentration of CHQ, which is taken up by and alkalinizes lysosomes. This compromises lysosomal function, in turn inhibiting lysosome-dependent clearance of autophagosomes and phagosomes; the altered levels of LC3B-II and SQSTM1 reflects autophagy initiation and would-be clearance over the period of CHQ treatment [47,49].

The top 2 panels in Figure 4a represent an immunoblot assay, probing with antibodies against SQSTM1 and MAP1LC3B, using proteins extracted from SLOS RPE and control RPE cells that had been cultured in the presence and absence of CHQ (150 μM) for 24 h (see *Methods*, below). Notably, under the conditions employed, we did not observe appreciable cell death due to CHQ treatment. Semiquantitative densitometry (Figure 4c) revealed the following: First, steady-state levels of LC3B-II (normalized to ACTB) in SLOS RPE were significantly higher (n = 3, $P < 0.05$, one-way ANOVA and Welch's t-test) compared to those in control RPE (Figure 4b). Second, concomitantly, there was a significant increase in SQSTM1 levels (normalized to ACTB), relative to control RPE SQSTM1 levels, at steady-state (Figure 4c). Taken together, the increased steady-state levels of LC3B-II and SQSTM1 may indicate decreased autophagic flux in SLOS RPE, as compared to control RPE. CHQ treatment increased LC3B-II levels ($P < 0.05$, one-way ANOVA and Welch's t-test) in both control and SLOS RPE cells (due to halted autophagosomal clearance). However, CHQ treatment did *not* significantly alter SQSTM1 levels in SLOS RPE (compared to untreated SLOS RPE, $P > 0.05$, one-way ANOVA and Welch's t-test), unlike the trend in treated *vs*. untreated control RPE (Figure 4c). This may be due to decreased autophagic flux and maximal accumulation of SQSTM1 at steady-state [50].

As mentioned above, LC3B-II is recruited to the phagophore membrane by ATG12 (autophagy related 12)–ATG5-mediated C-terminal lipidation of cytosolic LC3B-I with phosphatidylethanolamine (PE) [51], resulting in the formation of LC3B-II (which has increased hydrophobicity and therefore becomes noncovalently associated with the phagophore membrane) – *i.e*., the ATG12–ATG5 complex functions as an E3-ubiquitin ligase-like complex. Mutations in the *ATG5* gene have been shown to cause familial ataxia [52], a characteristic of which is chronically low steady-state levels of LC3B-II. We tested the possibility that ATG12–ATG5 levels might be altered in SLOS RPE, relative to those in control RPE cells. However, Western blot analysis (Figure 4a), probing with antibodies to ATG12–ATG5 complex, showed no appreciable differences between SLOS RPE and control RPE, with or without CHQ treatment (densitometric quantification not shown). Collectively, these observations suggest that SLOS RPE exhibit altered autophagic flux.

Multiple strategies have been utilized to monitor autophagosomes, including electron microscopy and tandem fluorescent-tagging of the autophagosome marker MAP1LC3B (RFP-

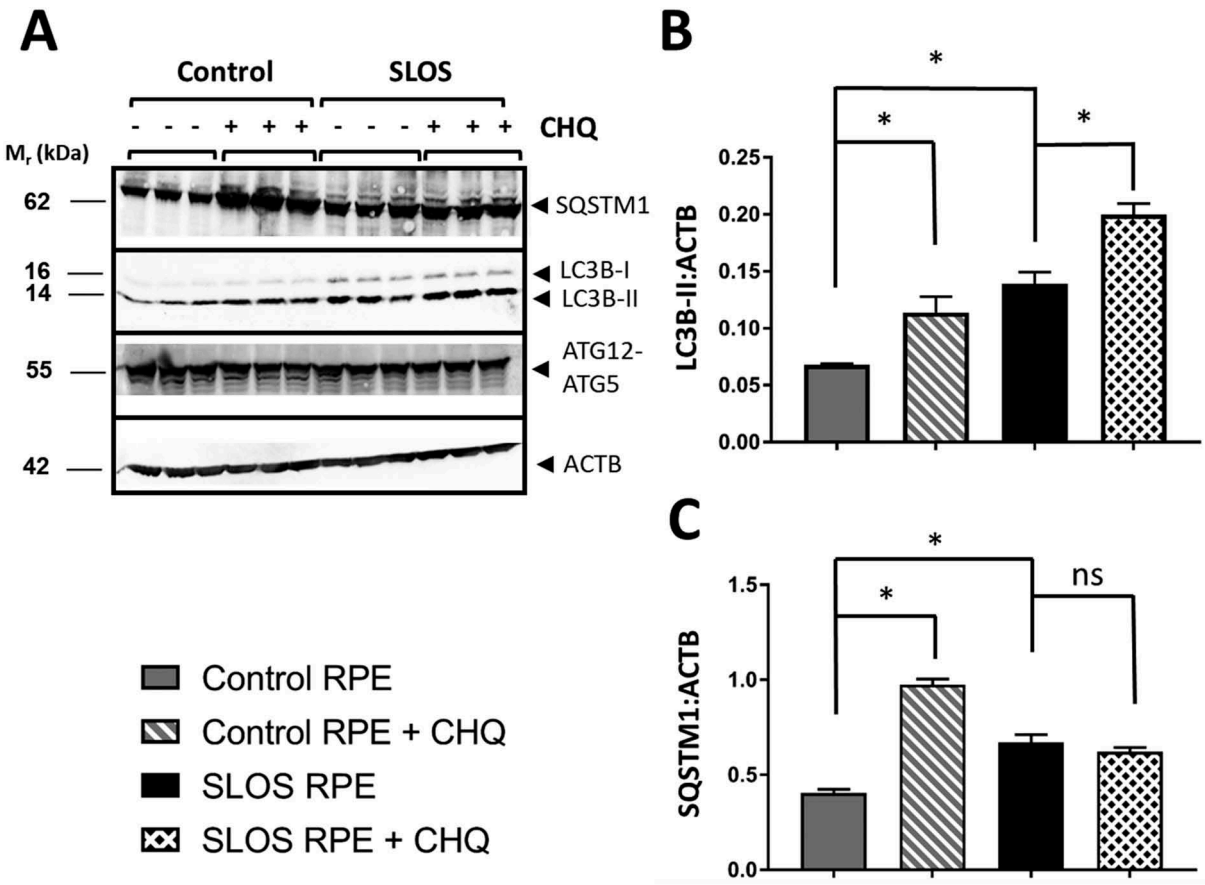

Figure 4. Monitoring autophagic flux. (**a**) Immunoblot analysis of steady-state levels of SQSTM1, LC3B-I and LC3B-II, and ATG12–ATG5 complex in control RPE and SLOS RPE cells under control conditions, as compared to incubation of both cell types in the presence of CHQ (150 μM, 24 h) (n = 3/treatment, normalized to ACTB). Values for apparent molecular mass (M_r, in kDa) of each protein are indicated on the left-hand side of the figure. Densitometric quantification of (**b**) LC3B-II and (**c**) SQSTM1 levels, normalized to ACTB levels, for both control and SLOS RPE cells, incubated with (cross-line bars) or without (solid bars) CHQ (See key inset). The steady-state level of LC3B-II in SLOS RPE was significantly higher compared to that of control RPE cells; this was accompanied by a significant ($P < 0.05$) increase in SQSTM1 levels in SLOS RPE, *vs.* control RPE cells. Upon CHQ treatment, significant increases in LC3B-II and SQSTM1 levels were observed in control RPE, but SLOS RPE exhibited an increase in LC3B-II levels only. Two-way ANOVA analysis: *$P < 0.05$; ns, not significant. Quantitatively, no appreciable difference was observed in ATG5 levels under normal or CHQ-treated conditions in SLOS RPE *vs.* control RPE cells.

GFP-LC3B) [53]. In this study, we utilized the convenient and effective tandem-tagging strategy (See *Methods*) to monitor the nature of the autophagic defect as observed in Figure 4. The RFP-GFP-LC3B approach takes advantage of differences in the pH sensitivity of the fluorescence of GFP (pKa 5.9) and RFP (pKa: 4.5): GFP is acid-sensitive, whereas RFP is not. Immature autophagosomes, which have not yet fused with acidic late endosomes or lysosomes, are expected to exhibit both GFP (green) and RFP (red) fluorescence (merged yellow signal when viewed by confocal fluorescence microscopy). Mature, acidified autolysosomes are expected to exhibit only the RFP (red) signal, due to acid-induced quenching of the GFP fluorescence. We transduced control and SLOS RPE cells with RFP-GFP-LC3B, and compared them with CHQ-treated control RPE cells as a positive control for accumulation of immature autophagosomes. Control RPE cells exhibited mostly RFP-positive signal, indicative of normal, active autophagosome maturation; by contrast, the SLOS RPE cells exhibited punctate vesicles that were both GFP- and RFP-positive, consistent with immature autophagosomes. CHQ-treated control and SLOS RPE cells exhibited, as expected, GFP- and RFP-positive punctate vesicles (Figure 5a). RFP-positive autophagosome puncta were counted in all groups/treatments (n = 100 each), and examined for GFP fluorescence. The bar graph shown in Figure 5b depicts the fraction of GFP-positive puncta compared to RFP-positive puncta, representing the percentage of immature autophagosomes in control and SLOS RPE cells. Also shown are the corresponding quantitative data for CHQ-treated cells. The percentage of GFP- and RFP-positive autophagosomes in SLOS RPE cells (49%), without CHQ treatment, was nearly 3-fold higher than that in control RPE cells (17%). CHQ treatment resulted in a substantial increase in GFP- and RFP-positive autophagosomes in both control (82%) and SLOS RPE cells (69%). Given that the lysosomal pH in SLOS RPE cells is within the normal physiological range (Figure 3), the data shown in Figure 5 suggest that the autophagic defect observed in SLOS RPE cells is due to defective autophagosome maturation or fusion with lysosomes.

Since the steady-state levels of LC3B-II and SQSTM1 were elevated in SLOS RPE compared to control RPE, and we observed accumulation of GFP- and RFP-positive immature autophagosomes in SLOS RPE cells, we predicted that SLOS RPE would exhibit defective degradation and clearance of

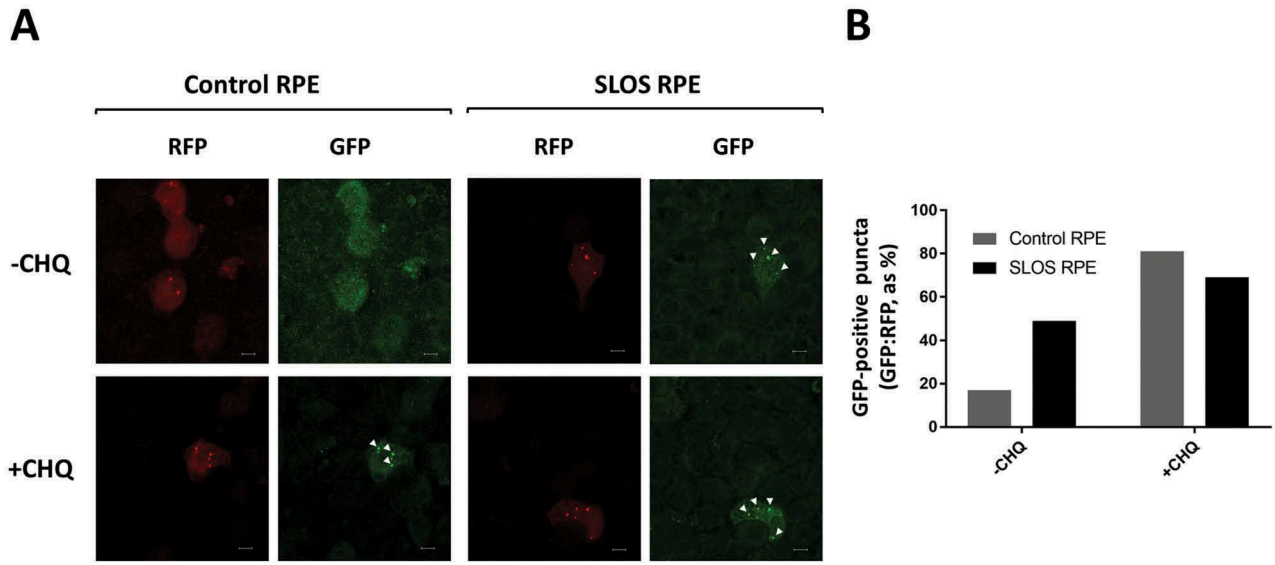

Figure 5. SLOS RPE cells are defective in phagosome maturation. (**a**) Control and SLOS RPE cells were transduced with RFP-GFP-LC3B and incubated in the presence (+ CHQ) and absence (-CHQ) of chloroquine. Control RPE cells exhibited mature phagosomes that were predominantly positive only for RFP (not GFP); when treated with CHQ, they exhibited accumulation of GFP- and RFP-positive puncta (white arrowheads), indicative of immature (unacidified) phagosomes. In contrast, SLOS RPE cells exhibited many GFP- and RFP-positive puncta without CHQ treatment, comparable to CHQ-treated cells. Scale bars: 5 μm. (**b**) Quantification of GFP- and RFP-positive puncta (n = 100/group/treatment) under conditions as in panel A. The ratio of GFP- to RFP-positive puncta (GFP:RFP) was calculated, and expressed as a percentage value, equating to the population of immature phagosomes.

retinal rod outer segment (ROS) membranes *in vitro*. Hence, control and SLOS RPE cells were incubated with purified bovine retinal ROS (5 particles/cell) for 2 h (to allow binding and phagocytosis of ROS), and then briefly rinsed with fresh culture medium and incubated further for 48 h (to allow sufficient time for heterophagic processing of the phagocytized ROS to occur). Following the incubation period, cells were harvested and the efficiency of ROS degradation was assessed by western blot analysis, probing the blots with antibodies raised against the C-terminal (1D4 epitope) domain of RHO (rhodopsin). The evidence-based rationale for this approach is as follows: Independent evidence suggests the onset of degradation of outer segment material upon acidification (due to lysosomal fusion) [54,55]. Because the C-terminal domain of RHO is exposed to lysosomal proteolytic attack at the cytoplasm-facing surface of the ROS disc membranes (in preference to the N-terminal domain at the luminal aspect of the discs), 1D4 degradation is the first step in the sequential phagolysosomal degradation of RHO in the RPE [56,57]. It follows that persistence of 1D4-positive material in the cells signifies defects in early processing of ROS (*i.e.*, merging of phagosomes with lysosomes), which also may indicate defective phagosomal trafficking of the exogenously supplied and ingested ROS material. As shown in Figure 6, the amount of residual 1D4-positive material in SLOS RPE cells was significantly greater than that observed in control RPE cells. Residual, undigested OS was estimated as the percentage of total RHO degraded at 48 h, with respect to the initial RHO content at 2 h (*i.e.*, the ratio of ACTB-normalized opsin 1D4 content at 48 h to that at 2 h, expressed as percentage). Residual 1D4-positive material after 48 h in SLOS RPE (88.2 ± 7.2%) was significantly higher compared to that in control RPE (31.8 ± 4; n = 3/group, $P < 0.05$) (Figure 6a,b). Immunohistochemical analysis of OS phagocytosis (Figure 6c) shows juxtaposition of successfully phagocytized 1D4-positive early phagosomes (red channel) with CTSD-positive lysosomes (green channel) after 2 h in control RPE cells (white arrows, 3D inset). SLOS RPE cells exhibited successful phagocytosis; however, 1D4-CTSD overlap was not readily observable. At 48 h, 1D4-positive immunostaining was no longer observable in control RPE cells, unlike SLOS RPE cells, which showed persistence of 1D4-positive material.

We hypothesized that the LC3-associated phagocytosis (LAP) clearance mechanism is also utilized in the clearance of heterophagic cargo by RPE cells *in vitro*. To test this, control and SLOS RPE cells were incubated in the presence or absence of 3-methyladenine (3-MA), an inhibitor of autophagy [58], followed by challenge with purified ROS membranes for 2 h and 48 h (again in the presence or absence of 3-MA), using the same protocol as described above. Cells were then rinsed and harvested at both time points, and subjected to western blot analysis, probing the blot with 1D4 monoclonal antibody as well as anti-ACTB. As shown in Fig. S6, the RHO content (normalized to ACTB) of untreated control RPE cells at 48 h post-challenge with ROS was about 4-fold lower than that at 2 h post-challenge, indicating that the degradative pathway was intact and functional. However, the normalized opsin content of control cells treated with 3-MA was comparable at 48 h post-challenge to the levels at 2 h post-challenge with ROS, indicating that 3-MA had effectively blocked the degradation of ingested ROS membranes. By contrast, the normalized RHO content of untreated SLOS RPE cells at 48-h post-challenge with ROS was only reduced by about 30% relative to that at 2 h post-challenge, consistent

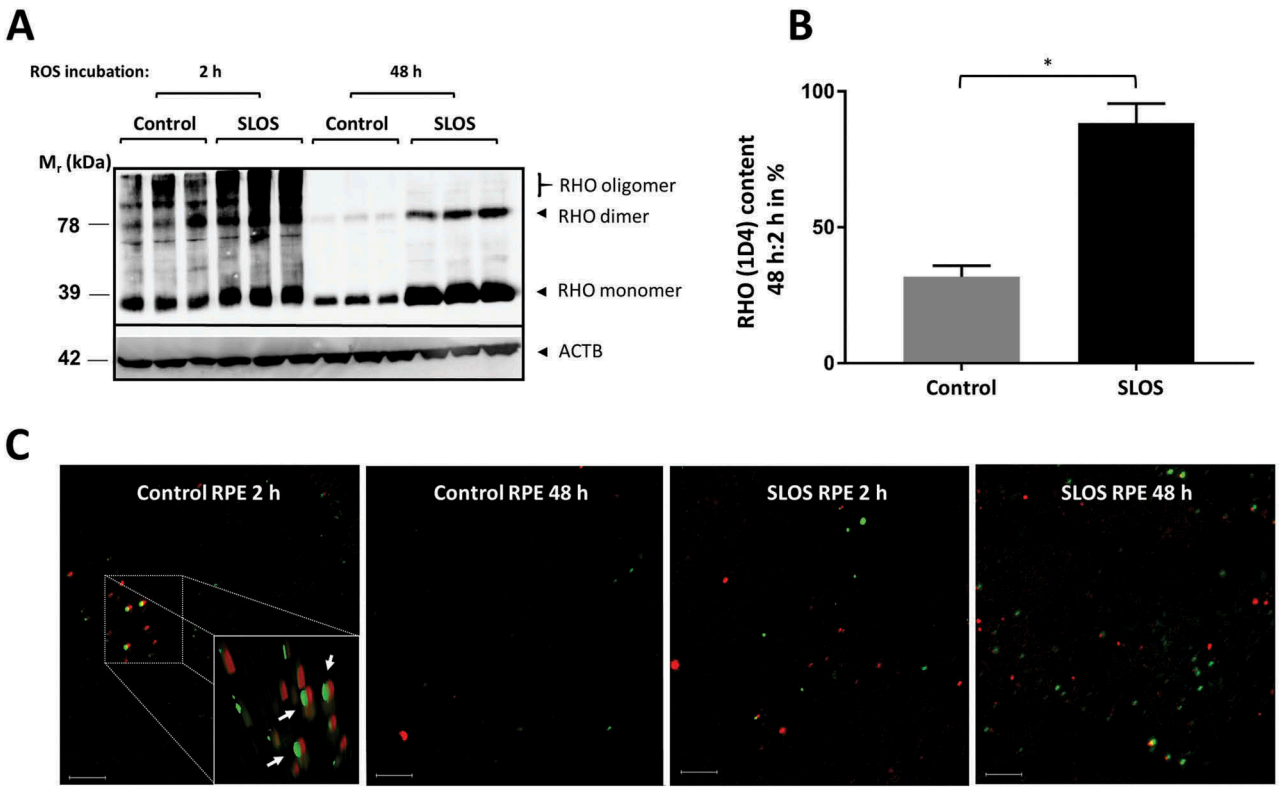

Figure 6. In vitro bovine ROS phagocytosis and degradation assay. (**a**) Western blot analysis of control and SLOS RPE cells (n = 3 per time point), incubated with purified bovine ROS for 2 h, then washed and either harvested immediately or incubated an additional 48 h. Cellular protein extracts at both time points were prepared and then electrophoresed and probed with 1D4 anti-RHO (1D4) monoclonal antibody to test for successful phagocytosis (at 2 h) and degradation (at 48 h). The migration positions corresponding to monomeric, dimeric and oligomeric forms of (rhod)opsin are indicated. Protein loading levels were validated using ACTB as a loading control. (**b**) Densitometric quantification of ROS degradation at 48 h, with respect to the initial phagocytic uptake. At 48 h, SLOS RPE cells exhibited persistence of undigested RHO carboxy terminus (~ 88% of initial phagocytized load at 2 h), as compared to control RPE cells, which exhibited ~ 30% residual ROS load at 48 h. (*$P < 0.05$, Welch unpaired t test). (**c**) Immunohistochemical analysis to monitor the maturation fate of phagocytized ROS (monitored using 1D4 antibody; red channel). Lysosomes (monitored using anti-CTSD; green channel) and 1D4-positive phagocytized ROS are juxtaposed 2 h after ROS challenge in control RPE cells (white arrows; 3-dimensional inset), and were successfully cleared by 48 h. In contrast, although SLOS RPE cells were able to bind and ingest ROS, neither early phagosome-lysosome juxtaposition nor subsequent degradation of 1D4-positive (ROS) material was observed by 48 h. Scale bar: 5 μm.

with defective degradation machinery. Treatment of SLOS RPE cells with 3-MA blocked even this modest reduction in opsin levels: the normalized opsin content was comparable at both 2-h and 48-h post-challenge with ROS. (Note: 3-MA did not perturb binding or phagocytosis of ROS.) These observations are consistent with our initial hypothesis.

Proteostasis, altered autophagic flux, and defective phagosome maturation, accompanied by the inability to degrade exogenously supplied ROS material are some of the key pathologic features of this novel *in vitro* SLOS RPE model. We hypothesize that these defects arise due to the defective DHCR7 activity and consequent accumulation of 7DHC and its derivative oxysterols through mechanisms yet to be elucidated [59,60].

Elevated ocular A2E and other bis-retinoids of RPE in SLOS rat model

We have previously shown that the RPE in the SLOS rat model exhibits marked accumulation of lipid-laden material and membranous inclusions – consistent in size and appearance with phagosomes derived from ingestion of shed ROS tips – compared to age-matched controls [13]. Based on this observation and a variety of studies by others [61], we hypothesized that the RPE in the SLOS rat model may contain substantially elevated amounts of A2E and other bisretinoids, relative to normal age-matched controls. In addition, since A2E and other bisretinoids are known to be cytotoxic to RPE cells *in vitro* and have been associated with a variety of processes that lead to retinal degeneration *in vivo* [62,63], we further hypothesized that this might be a significant contributing factor to the retinal degeneration observed in this animal model.

As shown in Figure 7, compared to age-matched control rat eyes, SLOS rat model posterior eyecups at 3 months of age exhibited the following fold-change increases ($P < 0.05$) in retinoids (Figure 7a): A2E, 1.52X; isoA2E, 2.20X; total A2Es, 1.71X; all-*trans* retinaldehyde, 1.57X. Representative reverse-phase UPLC chromatograms showing changes in bisretinoid levels are shown in Figure 7b. These results are consistent with our hypothesis, as stated above.

Given the finding of elevated bisretinoid levels (particularly of A2E, a prominent fluorophore component of RPE lipofuscin), we expected to observe increased autofluorescence in the RPE of SLOS rat eyes compared to age-matched controls when tissue sections were viewed by fluorescence microscopy (488 nm excitation, and 500 to 600 nm emission).

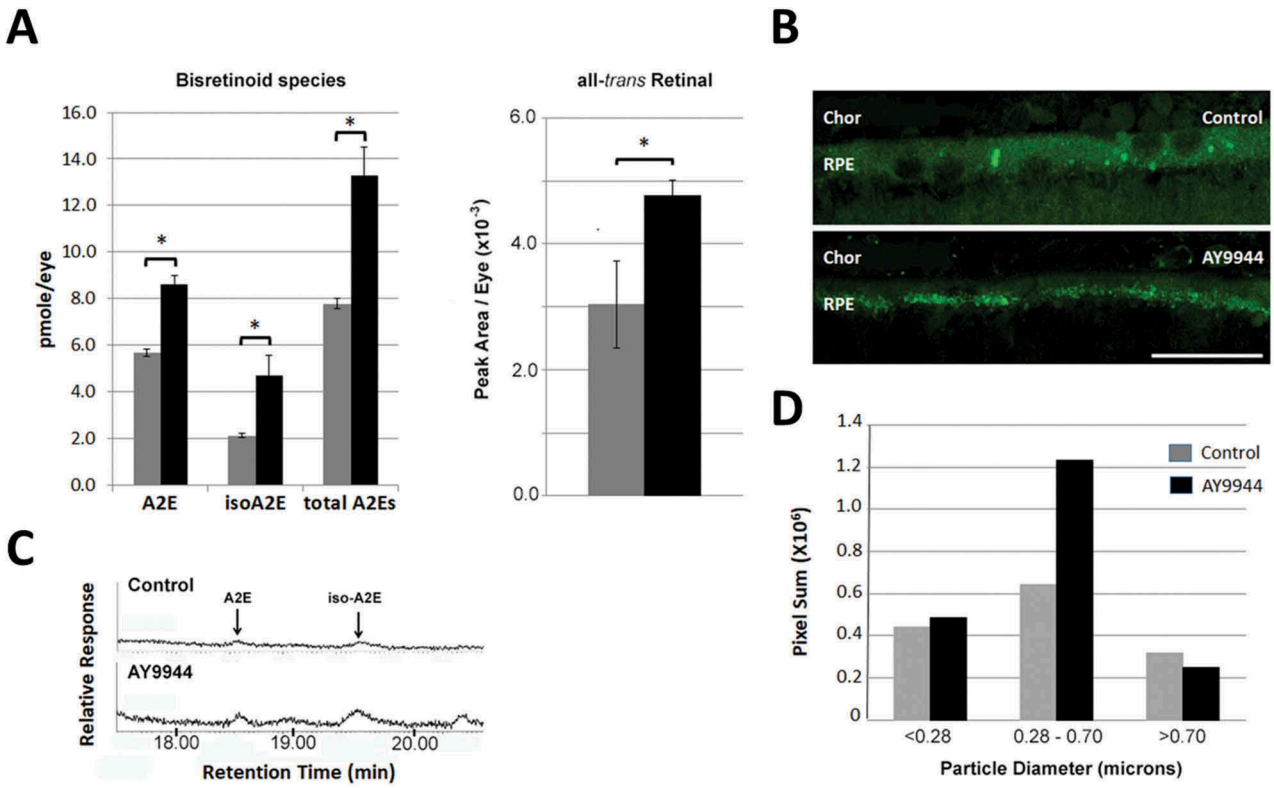

Figure 7. Correlation of bisretinoid levels with RPE autofluorescence in eyes from untreated (control) and AY9944-treated (SLOS) rats. (**a**) Quantification of bisretinoid species and all-*trans* retinaldehyde levels in eyes from untreated (*gray bars*) and AY9944-treated (*black bars*) rats (3 months postnatal). Posterior eyecups (*i.e.*, eyes minus anterior segment tissues) were extracted with organic solvents and the extracts analyzed by UPLC-MS (34). Extracts from AY9944 (SLOS) rat eyes contained significantly (*$P < 0.05$, n = 3) elevated levels of bisretinoid species and all-*trans* retinal, compared to eyes from untreated, age-matched (control) rats. (**b**) Representative reverse-phase UPLC chromatogram of lipid extracts of eyes from untreated (control) rats (*upper panel*) and SLOS (AY9944-treated) rats (*lower panel*). The chromatogram demonstrates detection and resolution of A2E and other bisretinoids (*e.g.*, iso-A2E); quantification of each component is determined by integrated peak area. (**c**) Representative confocal fluorescence micrographs depicting RPE autofluorescence in 3-month-old control (*upper panel*) and AY9944-treated (*lower panel*) rat eyes. Scale bar: 25 µm. (**d**) Pixel quantification of autofluorescence intensity observed in RPE in the representative confocal image shown in (**c**), measured as a function of particle diameter (in microns). Note the increased number of hyperfluorescent puncta in AY9944-treated RPE, particularly in the apical cytoplasm, compared to control RPE, consistent in size (0.28 to 0.70 µm diameter) and distribution with phagosome-derived material (*i.e.*, lipofuscin granules) [62] .

Representative images obtained by confocal fluorescence microscopy of cryosections of fixed eyes harvested from 3-month-old control and SLOS rats validated this expectation. Eyes were harvest 6 h into the light phase of the light-dark cycle, a time point by which most phagocytized ROS tips should have been degraded by the RPE phagolysosomal machinery [21,64]. A representative micrograph of the SLOS rat RPE (*lower panel*, Figure 7c) shows accumulation of numerous hyperfluorescent puncta in the apical cytoplasm. By contrast, the RPE cytoplasm of control rat eyes (*upper panel*, Figure 7c) exhibited mostly diffuse autofluorescence. Size-based quantitative image analysis of the autofluorescent puncta from a representative tissue specimen (Figure 7d) revealed a substantial increase (1.91-fold) in the number of puncta with diameters ranging from 0.28 to 0.70 µm. These observations are consistent with the original histological findings in this SLOS rat model, and further suggest that the heterophagic processing of phagocytized ROS tips is somehow hampered at an early stage of phagosome maturation.

Phagosomes in the RPE fail to fuse with lysosomes in vivo

As mentioned above, the sequential degradation of RHO/opsin can be used as an indicator to monitor phagosome maturation and concurrent OS clearance by RPE. The early phase in ROS clearance is characterized by the degradation of the cytosol-exposed C terminus of RHO (1D4 epitope) upon early endosome fusion with phagosomes [56]. By contrast, rhodopsin's N-terminal domain is located in the ROS disk lumen, thus inaccessible initially to proteolysis, and is degraded in a later stage of phagolysosomal processing. As a follow-up to our prior electron microscopic observations of the RPE in the SLOS rat model [11], we tested whether or not: a) accumulated phagosomes in the RPE are 1D4-immunopositive, and b) if the phagosomes fuse with lysosomes.

In agreement with our previous findings, we observed poor clearance of phagocytosed ROS (6 h post light onset) *in vivo* by the RPE of AY9944-treated Sprague Dawley rats (age: one month postnatal), relative to age-matched controls. Upon examination by confocal immunofluorescence microscopy, using antibodies raised against the 1D4 epitope of RHO, we observed persistence of 1D4-immunopositive ($1D4^+$) material in the RPE in SLOS rat eyes, while the RPE in age-matched control rats exhibited little or no $1D4^+$ immunoreactivity (**Figure 8**), the latter being consistent with the expected clearance of phagocytized ROS material at that time point in the light-dark cycle. Higher magnification micrographs further illustrate persistence of $1D4^+$ immunoreactivity in the apical

RPE cytoplasm, signifying retention of an intact RHO/opsin C-terminal domain in the phagosomes (Fig. S4). The C-terminal domain of RHO, which contains the epitope recognized by the 1D4 monoclonal antibody, is proteolytically degraded by the RPE heterophagic machinery upon early phagosome maturation [56]. Therefore, the finding of 1D4 + material suggests that RHO-containing phagosomes failed to mature and fuse with lysosomes (Figure 8, S4). We pursued this further using dual-label immunohistochemistry, using monospecific antibodies raised against the RHO C-terminal domain (1D4) and CTSD, a lysosomal protease. RPE cells in control rat eyes were essentially devoid of $1D4^{+}$ material (Figure 8), indicating no steady-state accumulation of rhodopsin, but exhibited a spatial distribution of CTSD-positive material (Figure 8, and higher magnification image in Fig. S4) consistent with that of lysosomes. By contrast, there were numerous focal clusters of $1D4^{+}$ material found in the RPE of SLOS model animals (Figure. 8 and S4), congruent in size and spatial distribution with early phagosomes, that were completely distinct and spatially segregated from the CTSD-positive material. These results are consistent with failure of (rhod)opsin-containing phagosomes in SLOS rat RPE cells to mature and fuse with lysosomes.

To rule out the possibility that the phagosome clearance defect observed in the SLOS AY9944 rat model *in vivo* might be due to unknown off-target effects of AY9944, we further tested for clearance of ROS material in a genetic mouse model of SLOS (bearing compound heterozygous mutations: T93M and deletion of exons 3–5 in *Dhcr7*) [65,66]. As shown in Fig. S5, the genetic murine model of SLOS exhibited a severe defect in the clearance of phagocytized ROS, relative to age and sex-matched controls – in strong agreement with the prior observations made using the AY9944 SLOS rat model. This finding, along with those previously described from *in vitro* and *in vivo* experiments, further validate the conclusion that defective cholesterol synthesis, as occurs in SLOS, leads to defects in RPE phagosomal maturation and fusion with lysosomes, with no discernable issues in binding or internalization of exogenous cargo.

Discussion

We have previously provided the first ultrastructural description of heterophagic defects in the RPE, upon perturbing the last step in cellular Chol synthesis [13]. Chol is a known structural component of phagosome membranes [67,68]. Recent reports concerning the functional role of Chol in autophagy and the phagolysosomal system (see below, and [42,69–73]) have prompted us to address the mechanism underlying the observed RPE pathology in the SLOS rat model. Furthermore, the fact that the RPE ultrastructural abnormalities exhibiting altered phagosome clearance in SLOS rat model precede any observable morphological or electrophysiological defects in the neural retina made us rethink our original assumptions that discounted, or presumed a secondary role, that these RPE defects might play in the retinal degeneration. More recently, 7DHC dose-dependent accumulation of autophagosomes in fibroblasts from multiple SLOS patients, has been observed [74]. The results of the present study provide preliminary mechanistic evidence for defective outer segment clearance upon 7DHC accumulation: failure of phagosomes to fuse with late endosomes or

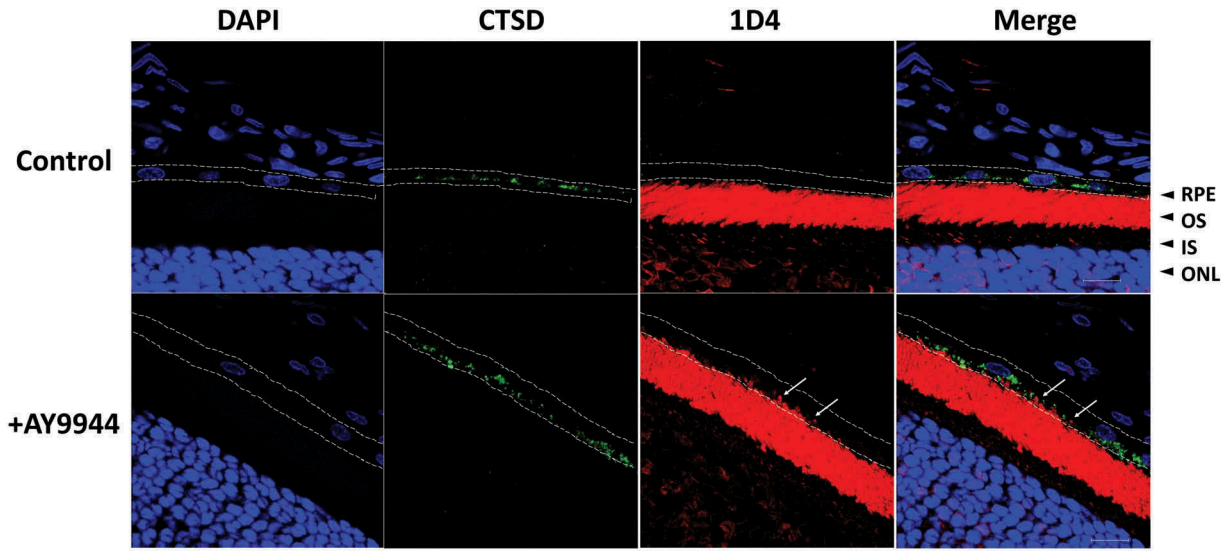

Figure 8. Accumulation of 1D4-positive phagosomes in the RPE of AY9944-treated animals, and their failure to fuse with lysosomes. Immunohistochemical localization of RHO C-terminal domain (detected by 1D4 monoclonal antibody and Alexa Fluor 647-conjugated secondary antibody; red pseudocolor) in RPE and outer retina of 1-month-old control and AY9944-treated Sprague-Dawley rats. Animals were maintained on a 12L:12D light-dark cycle (*ca.* 40 lux ambient light intensity), and eyes were harvested 6 h post light onset (*i.e.*, well after daily shedding, phagocytosis, and degradation of ROS tips by the RPE normally has occurred). Note the lack of 1D4-positive phagosomes in the RPE (demarcated by dashed lines) of the control eye (upper panels). However, the RPE layer in AY9944-treated rats (lower panels) exhibited substantial accumulation of 1D4-positive phagosomes, indicative of unprocessed C-terminal domain of RHO (white arrows). Dual-label immunohistochemical localization of RHO *vs.* CTSD (the latter detected with a rabbit polyclonal anti-CTSD antibody and Alexa Fluor 568-conjugated secondary antibody; green pseudocolor) shows that the accumulated 1D4-positive phagosomes in the RPE of AY9944-treated rats (arrows, merge panel) do not colocalize with CTSD immunoreactivity, and that CTSD immunoreactivity is more intense in the RPE of AY9944-treated rats, relative to that in control animals, in agreement with our previous study [14]. Scale bars: 10 μm. See Fig. S4 for higher magnification images.

lysosomes. To the extent that the AY9944-induced rat model and the genetic mouse model of SLOS reliably reflect the pathobiology of the human genetic disease, a more fulsome understanding of the RPE pathology observed in the SLOS rat model may provide useful insights into the SLOS-associated retinopathy.

Ipsc-derived SLOS RPE as an in vitro model

The utility of SLOS iPSCs to design reliable *in vitro* models of this complex metabolic disorder was recently demonstrated [28]. The iPSC-derived SLOS RPE *in vitro* model has certain advantages over the 2 other *in vitro* approaches currently in use: transient treatment with 7DHC-derived oxysterol, or AY9944 treatment of normal cells. Exogenous oxysterol treatment of RPE cells cannot account for the most significant biochemical defect in SLOS, *i.e.*, accumulation of *de novo* synthesized 7DHC. Short-term, exogenous oxysterol treatment may require exaggerated concentrations to trigger cell pathology or cell death. While AY9944 treatment of cells may offer a tractable approach, one cannot obviate potential off-target pharmacological effects, nor can it predictably replicate the extent of DHCR7 inhibition that occurs *in vivo* in the SLOS rat model. Complete inhibition of Chol synthesis is not representative of the human disease with mutant *DHCR7*. Gene product of mutant *DHCR7* isoforms possess hampered, rather than absent (null), enzymatic activity, resulting in fractional 7DHC:Chol mole ratios in plasma and bodily tissues [3]. The *in vitro* model employed in this study involves 2 of the most commonly observed disease-causing mutations in SLOS, and faithfully mimics the typical sterol profiles observed in cells and tissues from SLOS patients bearing the same compound heterozygous mutations (*i.e.*, about 40% of cellular sterol content in SLOS RPE was 7DHC) [10], while generating 7DHC-derived oxysterols (unpublished result). Patients with T93M and IVS8-1G> C compound heterozygous mutation exhibit serum cholesterol percentage between 38.4% to 62.3%, with clinical severity scores ranging from 74 to 26 (as well as postnatal lethality) [3]. Detailed transcriptomic analysis of this novel *in vitro* resource (in progress) is expected to shed light on the pertinent pathological mechanisms involved.

Morphologically, the SLOS RPE cells exhibited the polygonal shape characteristic of RPE cells and formed confluent monolayers with a cobblestone-like appearance typical of RPE cells; however, their TJP1-positive cell borders often appeared to be somewhat disorganized (Figure 1f). We observed punctate cytoplasmic immunohistochemical staining of TJP1, along with stable cell border decoration in SLOS RPE cells. Whether the cytoplasmic, punctate appearance of TJP1-positive structure in SLOS RPE cells occurs due to defects in trafficking of elements of the junctional complex or, alternatively, to autophagy-dependent degradation remains to be understood [75,76]. However, this defect does not affect the ability of SLOS RPE cells to form an electrically tight monolayer. SLOS RPE cells were comparable to control RPE cells in their capacity to successfully establish confluent monolayers on laminin-coated permeable membrane inserts, resulting in the development of transepithelial resistance (TEER) values > 300 $\Omega^{*}cm^{2}$ within 2–3 weeks of seeding (Figure 1g). In the current study, we adapted a previously established strategy (low-calcium medium) to propagate and subculture control and SLOS RPE cells [35,36,77]. This strategy avoids trypsin treatment to dislodge cells from their culture substrate for serial passaging. Utilizing this approach, we have verified that our RPE cell cultures express RPE-specific markers up until at least passage number 6 at the transcriptional (Figure 1i,j) and translational (Figure 1h) levels.

The LDL receptor-mediated Chol uptake mechanism in the RPE has been observed *in vivo* and *in vitro* [78,79]. This is further corroborated by the accumulation of Chol in lysosomes of the RPE in Niemann Pick type C-1 (*npc1*) knockout mice [80]. It is reasonable to expect that RPE cells in SLOS animal models and in SLOS patients would import blood-borne 7DHC and oxLDL (packaged by the liver in lipoprotein particles), in addition to engaging in endogenous active *de novo* 7DHC synthesis. Our iPSC-derived RPE cell culture model mimics the defective *de novo* synthesis of Chol (a key biochemical hallmark of SLOS), while generating 7DHC and 7DHC-specific oxysterols (unpublished results), but does not account for LDL-bound 7DHC and/or oxLDL supply expected *in vivo*. As part of our culture media formulations that largely replaced serum with more defined components, we provided low levels of exogenous cholesterol (in the form of 0.9% BCS) in our culture system to maximize the effect of the onboard *DHCR7* mutations on the biosynthetic machinery.

Elevated lipofuscin in the SLOS rat model

Autophagy is an evolutionarily conserved cellular homeostatic process required to remove large, endogenous cellular debris, such as damaged organelles (*e.g.*, mitochondria, peroxisomes, ER membranes, etc.) and protein aggregates (reviewed in [81,82]). Chronic downregulation of autophagy in long-lived, post-mitotic cells, such as neurons, cardiac myocytes, and RPE cells (reviewed in [83–87]), leads to accumulation of damaged organelles, increased oxidative stress, leading to accelerated aging and cell death [88,89]. The RPE is additionally challenged with photooxidative stress associated with bisretinoid accumulation [51] and diurnal phagocytic degradation of OS membranes shed by the adjacent photoreceptor cells [21,90]. OS membranes, which are enriched in phospholipids containing oxygen-labile polyunsaturated fatty acids (notably, docosahexaenoic acid (C22:6,n-3)) and all-*trans* retinaldehyde (the isomerized chromophore of the visual pigment, rhodopsin, hydrolytically liberated from the protein following absorption of light by rhodopsin) are the major precursors responsible of the formation of bisretinoid lipofuscin in photoreceptor OS [91].

Lipofuscin is a compositionally complex material that is essentially devoid of proteins, but consists of A2E and other bisretinoids (which account for the autofluorescent nature of lipofuscin), in addition to their oxidized forms, and its accumulation is an indicator of aging in the RPE [61,92]. *In vitro* evidence suggests that lipofuscin components, including A2E, can inhibit phagosome formation and phagosome trafficking in the RPE [31]. A2E also can inhibit Chol metabolism and

retard Chol efflux in RPE cells, which in turn can further exert deleterious effects on the phagolysosomal machinery of the RPE [31,93]. In this study, we found increased levels of autofluorescent, lipofuscin-like material in the apical cytoplasm of the RPE, as well as increased levels of bisretinoids (A2E and related molecules, which initially form in the photoreceptor OS), in the eyes of the SLOS rat model, compared to eyes from normal, age-matched control rats. We observed this finding in animals that were 3 postnatal months of age, a time point at which advanced panretinal degeneration is observed. We have not investigated bisretinoid accumulation at earlier time points. However, defective clearance of phagocytized photoreceptor OS membranes and direct inhibition of autophagy in RPE cells has been associated with lipofuscin (or lipofuscin-like material) accumulation [94–96]. In the SLOS rat model employed here, the increased steady-state load of undigested OS may provide a local, concentrated depot of the 2 essential building blocks required to make A2E and other bisretinoids: all-*trans* retinaldehyde (from photo-bleached rhodopsin) and ethanolamine (from PE, the dominant glycerophospholipid component of OS membranes). Concomitantly, bisretinoids, at sufficiently high levels, can be cytotoxic and can accelerate RPE pathology [51]. Further elucidation of the interplay between heterophagy and bisretinoids in the context of the SLOS-associated pathology remains to be pursued.

Parallel evidence for the requirement of chol in phagosome maturation

Chol is a key component of the detergent-resistant membrane (DRM) domains, (*i.e.* 'lipid rafts') that form transient, spatially segregated membrane microdomains in biological membranes, supporting a variety of critical cell signaling processes (reviewed in [97,98]). Autophagy is dysfunctional in several human disorders and animal models involving altered Chol metabolism, trafficking and homeostasis. For example, in NPC1 disease, a lysosomal Chol storage disorder, autophagosomes fail to fuse with Chol-laden late endosomes [99]. Similar manifestations have been observed in a widely accepted *in vitro* model of atherosclerosis, involving treatment of peripheral macrophages with U18666A, which binds to the NPC1 protein and inhibits Chol trafficking from lysosomes to the endoplasmic reticulum (ER) [100,101]. In the present study, we have described the effects of distal inhibition of Chol biosynthesis (at the level of DHCR7, the final enzymatic step) on autophagy, further corroborating prior studies (discussed below) that have implicated a requirement for Chol in the mechanism of autophagic flux.

Freeze-fracture and transmission electron microscopic studies of filipin binding to phagosomal vacuoles have demonstrated the differential distribution of Chol in phagosomes [68]. The membrane content of Chol and sphingomyelin (the principle lipid components of lipid rafts) is about 1.5- to 1.75-fold higher in phagolysosomes than in nascent phagosomes [72]. The RPE phagosomal envelope (containing membranes originating from distal OS tips) is relatively enriched in Chol, while the distal portion of the OS itself exhibits relatively sparse Chol content [67]. Recent investigations on the regulatory role of lipid rafts in phagosome maturation have shown that dynein motors cluster in the lipid rafts of maturing phagosomes and orchestrate unidirectional, retrograde phagosome trafficking towards microtubule 'minus' end to fuse with lysosomes [72]. OSBPL1A/ORP1L (oxysterol binding protein like 1A), a component of the Chol/oxysterol-sensing machinery in cells, recruits the RAB7 small GTPase and dynein motors to the phagosomal membrane in the presence of Chol [73,102]. Simultaneous LDL-starvation and statin treatment *in vitro* retards phagosome motility, and hence, phagosome maturation [73]. Cyclodextrin-mediated depletion of Chol from phagosomal membranes retards late endosome and lysosome fusion by inhibiting phagosome motility [71,72]. Knowledge about the direct involvement of Chol in autophagy stems from studies based on cell culture, purified organelles, upstream pharmacological inhibition of rate-limiting step in sterol biosynthesis, and cyclodextrin-mediated disruption of lipid rafts. The current SLOS study is the first *in vivo* investigation of LAP-dependent RPE photoreceptor outer segment clearance upon distal inhibition of Chol synthesis. The accumulation of 1D4-positive, CTSD-negative ROS material in the RPE *in vivo* is a direct indication of stagnation of phagosomes at an early stage of phagosome processing. Oxidation of 7DHC to form 7DHC-specific oxysterols may also contribute to defective phagosome maturation. This is in agreement with a study by Hoppe et al. [103], which reports defective phagosome maturation in RPE loaded with oxLDL.

Chol colocalizes with LC3B-II, the lipidated, membrane-associated form of LC3B, a membrane marker of autophagosomes [100]. LC3B-I (cytosolic form) is conjugated with PE to form LC3B-II by the action of the ATG12–ATG5 complex. RPE-specific *atg5* knockout results in halted clearance of OS load, suggesting RPE clearance involves LC3-associated phagocytosis (LAP) [20,26]. LC3B-II levels in the RPE undergo diurnal changes, exhibiting peak levels that correspond to maximal phagocytic activity (*i.e.*, about 1 h post-light onset) [104]. The baseline autophagic function of LC3B-II is to recruit SQSTM1-bound ubiquitinated cargo to phagosomes for lysosomal degradation [47]. Hence, under normal circumstances, the cargo and its chaperone (SQSTM1) are degraded via the phagolysosomal machinery, so steady-state levels of SQSTM1 (and ubiquitinated proteins) are low [47]. However, in our cultured SLOS RPE cells, the steady-state levels of ubiquitinated proteins, LC3B-II, SQSTM1, and undigested 1D4-positive material (undegraded visual pigment in the ROS) were significantly higher, compared to those in control RPE, indicating proteostasis as well as defective processing and maturation of autophagosomes, as well as heterophagosomes. Defective phagosome maturation and LC3-associated phagocytosis in SLOS RPE was further evidenced as accumulation of GFP- and RFP-positive phagosomes (in RFP-GFP-LC3B transduced cells), accumulation of 1D4-positive material, and lack of juxtaposition of 1D4-positive material and (CTSD-positive) lysosomes upon challenge with bovine ROS membranes.

7DHC readily undergoes free-radical (nonenzymatic)-mediated, as well as cytochrome P450-enzymatic, oxidation to give rise to a variety of 7DHC-specific oxysterols [7,105]. In the present study, we demonstrated that SLOS RPE cells

synthesize and accumulate 7DHC. We have recently verified the generation of 7DHC-derived oxysterols in the SLOS RPE cells (unpublished result), similar to what has been observed in SLOS fibroblasts [105], as well as what we've previously documented using the SLOS rat model [8,106]. We also observed elevated steady-state levels of ubiquitinated proteins in our *in vitro* model. Multiple factors may contribute to the occurrence of proteostasis; the mechanisms involved in the present case remain to be elucidated. While increased steady-state level of polyubiquitinated proteins may be suggestive of increased oxidative damage to cellular proteins due to elevated oxidative stress (unpublished results), it is plausible, alternatively, that there was decreased clearance of the ubiquitinated proteins by the 26S proteasomal system and/or SQSTM1-bound phagosomal cargo. Proteostasis in post-mitotic cells, such as neurons, RPE cells, and cardiomyocytes, is reflective of cellular pathology. Accumulation of ubiquitinated proteins in SLOS RPE cells, as compared to controls, should be considered a key feature of the RPE pathology.

Role of phagosome maturation in SLOS RPE pathology

We investigated the possible contribution of diminished lysosomal function to the RPE pathology observed in the SLOS rat model. However, the results obtained by measuring lysosomal pH as well as CTSD activity in cultured SLOS RPE indicated that, contrary to our alternative hypothesis, lysosomal function was *not* compromised. We considered the possibility that AY9944 itself (a quaternary amine, hence a base) might directly alkalinize lysosomes in the rat model; however, empirically, we found that even at a concentration of 30 μM (which is far greater than what would be achieved *in vivo*), AY9944 treatment of ARPE-19 cells failed to alter lysosomal pH (data not shown). We were surprised that the presence of delipidated serum in the culture medium led to a statistically significant elevation in lysosomal pH (by ~ 0.15 pH units), compared to using normal levels of serum. While the exact mechanism underlying this effect remains to be determined, it represents only a very minor alkalinizing effect, and the resulting lysosomal pH was still within the physiological range. We are unaware of prior reports concerning this effect of delipidated serum on lysosomal pH in cultured cells. Therefore, the endogenous formation and accumulation of 7DHC, *per se*, most likely does *not* lead to significant alterations in lysosomal function. In another study [107], it has been demonstrated that skin fibroblasts derived from SLOS patients also exhibited unesterified sterol accumulation, reminiscent of what occurs in Niemann-Pick type C-1 (NPC1) disease (which is characterized by accumulation of unesterified Chol in the lysosomal lumen). Lysosomal pH is not altered in NPC1 disease [108]. Therefore, altering Chol synthesis or its trafficking may not affect lysosomal pH directly.

Our *in vitro* model system does not incorporate, or address, the potential effects of exogenous LDL-bound 7DHC or oxLDL on RPE lysosome health. This seeming drawback can be more fully addressed in the SLOS animal model (where cells import 7DHC-laden LDL particles) by testing the colocalization of phagocytized material with lysosomes. Had we observed colocalization of 1D4-containing phagocytized material with the lysosomes, persisting 6 h into the light phase of the light-dark cycle, we would have attributed the phagocytic defect to dysfunctional lysosomal activity. However, the accumulated OS cargo was immunopositive for the 1D4 (RHO C-terminal) epitope and did not colocalize with lysosomes (as represented by CTSD immunoreactivity), essentially exhibiting characteristics of early phagosomes in the RPE [56]. Therefore, we attribute the failure of heterophagic RPE clearance in SLOS RPE to defective phagosome maturation. The apparent failure of phagosomes to fuse with lysosomes limits our ability to predict lysosomal function *in vivo*. We cannot discount the possibility of lysosomal alkanization *in vivo*, because it's known that chronic loading of macrophages with oxLDL can lead to lysosomal alkalinization [109]. The other possible mechanism for retarded phagosome maturation could be perturbation of phagosome lipid rafts, and downstream signaling, by 7DHC-derived oxysterols, which in turn may affect phagosome mobility and processing. We have discounted the possibility of AY9944-induced, off-target perturbation of autophagy in the AY9944-induced SLOS rat model by testing phagocytic clearance in a genetic murine model of SLOS (*Dhcr7*^{T93M}/ΔExon3-5). This mouse model (at postnatal week 16) [serum 7DHC:Chol ratio of 0.1 [65,110]] also exhibits hindered clearance of photoreceptor outer segments, strongly suggesting that the observed phagocytic clearance defect is a consequence of altered sterol synthesis and aberrant steady-state accumulation of 7DHC and biogenically related oxysterols in the RPE as a direct consequence of DHCR7 inhibition.

Phagosome clearance was inhibited by CHQ-induced alkalinization of lysosomes. We quantified protein levels of the autophagic markers LC3B-II and SQSTM1 in both normal steady-state and CHQ-treated conditions. A significant increase in steady-state LC3B-II levels was accompanied by elevated SQSTM1 levels in SLOS RPE, compared to control RPE cells. Upon CHQ treatment, LC3B-II accumulation in SLOS RPE was comparable to that observed in control RPE cells, suggesting unhindered activation of autophagy. CHQ treatment, while inducing an increase in LC3B-II levels in SLOS RPE cells, did not alter SQSTM1 levels. Mizushima et al. [50] have previously demonstrated similar trends in LC3B-II and SQSTM1 levels upon CHQ treatment of amino acid-starved fibroblasts. This is further a reflection of stagnant autophagy, as the model [50] suggests that the amino acids derived from lysosomal degradation of proteins are utilized to synthesize new SQSTM1 protein. These specific signatures of alteration in autophagy flux, alongside the accumulation of GFP and RFP-positive immature phagosomes in SLOS RPE, and accumulation of 1D4-positive material *in vitro* and *in vivo* models, indicate that LC3-convergent mechanisms of autophagy and LAP are defective at the level of phagolysosome formation. The role and regulation of LC3-associated phagocytosis in this pathology remains to be studied [111].

In conclusion, the current work has provided new insights into the nature of the RPE pathology observed in the AY9944-induced SLOS rat model, pinpointing the defect to phagosome maturation and contributing further to the existing literature that points to an important role for Chol in that process. Further investigation into the specific mechanisms of

the phagosome maturation defect may reveal new therapeutic targets for the treatment of SLOS and related Chol pathway disorders, for which no effective therapies currently exist.

Materials and methods

Materials and reagents

Unless otherwise specified, common laboratory chemicals, reagents, enzymes, and routine tissue culture reagents were used as purchased from Sigma-Aldrich. Organic solvents for lipid extraction and HPLC analysis were of the highest analytical grade or 'HPLC grade' (Thermo Fisher Scientific). AY9944 (*trans*-1,4-bis[2-chlorobenzyl aminoethyl] cyclohexane dihydrochloride) was custom synthesized, recrystallized to homogeneity, and the structure and purity verified by HPLC, LC–MS, NMR, and UV–VIS spectroscopy (Vanderbilt University Chemistry Core), in comparison with an authentic sample of AY9944 (a generous gift from Wyeth-Ayerst Research). Authentic chromatographic standards of Chol and 7DHC were obtained from Research Plus; 7DHC was purified, as needed, by repeated recrystallization prior to use (confirmed purity > 99%, by HPLC). All reagents and materials utilized for SDS-PAGE and western blot analyses were obtained from Bio-Rad Laboratories. Cell culture media and plasticware (Falcon™) and all other general lab supplies were obtained from Thermo Fisher Scientific, unless otherwise indicated. Dulbecco modified Eagle medium (DMEM) with HEPES (Sigma-Aldrich, D5546), DMEM without calcium chloride (ThermoFisher Scientific, 21,068,028). KBM-Gold™ (keratinocyte basal medium, calcium ion-free; Lonza, 192,151) and bovine calf serum (Hyclone Laboratories, SH30073) were purchased as indicated.

Cells and cell culture

Induced pluripotent stem cells (iPSCs; line 'CWI', a generous gift from Drs. Kevin Francis and F.D. Porter, NIH/NICHD) were generated from dermal fibroblasts obtained from a clinically diagnosed, well-characterized SLOS patient (6-day-old, male) harboring known disease-causing *DHCR7* mutations (T93M and IVS8-1G> C compound heterozygous mutations) [28]. The iPSCs were further differentiated to generate RPE cells ('SLOS RPE') harboring the same *DHCR7* mutations (fee-for-service; Neural Stem Cell Institute, Rensselaer, NY, USA). iPSCs generated from human foreskin fibroblasts obtained from a normal neonatal male subject (line ATCC-Dys0100; ATCC, ACS-1019™) were differentiated to RPE cells using the same methods [112–114] (fee-for-service; Columbia University Stem Cell Core Facility, New York, NY, USA), and served as 'control RPE' cells. Alternatively, in some experiments (specifically noted in the *Results* section), RPE cells differentiated from normal human embryonic stem cells (hesRPE, strain En74, derived from the h9 HsESC line, NIH registration number 0062; a generous gift of Dr. Lincoln V. Johnson, UCSB, Santa Barbara, CA, USA) were utilized as controls, designated 'nhRPE' cells.

The general procedures utilized for culture and treatment of RPE cells were as described in detail previously [115]. Passage 3 control and SLOS RPE cells were seeded onto 60-mm diameter culture dishes (~ 100,000 cells/ml, total volume of 4 ml) or 4-well Falcon™ culture slides coated with poly-L-ornithine or iMatrix-511® (recombinant laminin 511-E8 fragment; Takara Bio Inc., T301) (~ 150,000 cells/ml, total volume of 1 ml), in 'low-calcium' medium (1:1 calcium-free DMEM:KBM Gold® basal medium, $[Ca^{2+}]$ < 0.1 mM, supplemented with 1% [v:v] BCS [Hyclone Laboratories, SH30073], and 0.5% [v:v] bovine retinal extract [BRE; Animal Technologies incorporated, Tyler, TX]). RPE cells were proliferative under low-calcium conditions, generating both nonadherent cells ('floaters') from adherent RPE monolayers; 'floaters' were collected up to 2 weeks after initial seeding, and then reseeded onto new 60-mm dishes (maintained in culture up to passage 6). Confluent RPE monolayers were switched to 'high-calcium' medium ($[Ca^{2+}]$ adjusted to 0.45 mM and supplemented with 0.9% BCS and 0.25% BRE by substituting an appropriate volume of HEPES-buffered DMEM) [36,77]. Stable, confluent control and SLOS RPE monolayer cultures were maintained for 2 to 3 months, under humidified 94% O_2:6% CO_2 atmosphere at 36.5°C, with retention of characteristic RPE morphology, viability, and cellular integrity. For routine inspection and imaging, cell cultures were viewed using an Axiovert 25 CFL inverted photomicroscope (Carl Zeiss Microscopy LLC, Thornwood, NY, USA), equipped with an Evolution™ MP digital CCD 5.0 MP camera (MediaCybernetics, Rockville, MD, USA); digital images were captured and stored as .tif files on a standard PC computer (Dell).

For verification of on-board 7DHC synthesis and accumulation in SLOS RPE, cells were first seeded in low calcium medium. When the cells attained confluence, they were switched to, and maintained in, high calcium medium, supplemented with 0.9% BCS, for approximately 2 mo. To verify the functionality of the endogenous, defective DHCR7, parallel cultures were switched to high calcium medium, supplemented with 0.9% delipidated BCS, for 2 weeks, before harvesting the cells for Chol and 7DHC quantification.

For chloroquine (CHQ) treatment experiments, freshly made chloroquine diphosphate stock (15 mM in water, filter-sterilized; 100X stock; Sigma Aldrich, C6628) was diluted into appropriate volumes of high-calcium medium. Control and SLOS RPE cells (3-month-old cultures) were switched to high-calcium medium containing 150 μM CHQ and maintained for 24 h under standard conditions (see above). Parallel negative control cultures were switched to fresh high-calcium medium (no CHQ) to ensure that autophagy was not aberrantly upregulated due to lack of requisite nutrition.

For 3-methyladenine (3-MA; Cayman Chemical, 5142–23-4) treatment experiments, cells were incubated as described above in the presence ('treated') or absence ('untreated') of 15 mM 3-MA for 4 h, followed by 2 h of challenge with bovine ROS membranes (in the presence or absence of 7.5 mM 3-MA). After ROS challenge, cells were quickly rinsed with fresh medium, and allowed to incubate further for 48 h in the presence or absence of 7.5 mM 3-MA (3-MA concentration was reduced from the intial 15 mM to 7.5 mM to preserve cellular viability over the subsequent 48-h time

course). Cells were then rinsed, harvested, and subjected to western blot analysis.

For experiments involving immunohistochemical analyses (see below), RPE cells were cultured for 2–3 months on glass chamberslides coated with poly-L-ornithine and iMatrix-511®. Alternatively, cells were cultured on Rinzl plastic coverslips (Electron Microscopy Sciences, 72,261–22). Specimens were then treated as described below, probing with various primary and *secondary* antibodies, followed by imaging using scanning laser confocal fluorescence microscopy (additional details in *Results* and figure legends).

Pharmacological and genetic SLOS rodent models

The *in vitro* cell culture experiments were complemented by *in vivo* experiments employing rodent models of SLOS. The pharmacological SLOS rat model employed was as described in detail previously [11]. In brief, pregnant Sprague-Dawley dams (6-days sperm-positive; ENVIGO (formerly Harlan Labs)) were administered AY9944 via subcutaneously-implanted Alzet® osmotic pumps (DURECT Corp.) during the second and third gestational weeks; thereafter, rat pups were given subcutaneous injections of AY9944 (30 mg/kg, in phosphate-buffered saline [PBS; ThermoFisher Scientific, AM9625]) starting on postnatal day one, 3 times per week, throughout their life span (up to 3 months of age). Animals were maintained on a standard rodent diet, which is plant-based and, hence, Chol-free (Teklad, ENVIGO). Age/sex-matched untreated rats from parallel litters served as controls. Animals were maintained on a 12-h light:12-h dark cyclic light schedule (20 to 40 lux ambient light intensity at cage level), at 22 to 25°C, and typically were sacrificed 6 h into the light phase. All procedures conformed to the National Research Council's *Guide for the Care and Use of Laboratory Animals* (https://grants.nih.gov/grants/olaw/Guide-for-the-Care-and-use-of-laboratory-animals.pdf). Animals were euthanized by CO_2 exposure in a closed, plexiglass chamber, followed by cervical dislocation, in accordance with the procedures proscribed by the *AVMA Guidelines for the Euthanasia of Animals* (2013 Edition; https://www.avma.org/KB/Policies/Documents/euthanasia.pdf).

Eyes from a genetic mouse model of SLOS (*Dhcr7*^{T93M}/ΔExon3-5) [65,66], fixed in buffered paraformaldehyde, were obtained from Drs. Christopher Wassif and Forbes D. Porter (NIH/NICHD, Bethesda, MD). The methods employed for processing of fixed ocular tissues from both rat and mouse models are described below.

Sterol composition analysis

For this preliminary experiment aimed at verifying the catalytic inefficiency of DHCR7, sterol content of SLOS RPE was compared with HsESC-derived control RPE (nhRPE). Stable (*ca.* 2-month-old) monolayer cultures of nhRPE and SLOS RPE cells were switched from their standard culture medium (see above) to medium containing 0.9% (v:v) delipidated (*i.e.* sterol-depleted) BCS (prepared as described elsewhere [116]), and maintained for 2 weeks [see *Discussion* for rationale]. We verified that the delipidation protocol removes > 98% of the Chol from the BCS (see **Fig. S2A**). The culture medium was then aspirated, cells were rinsed 3 times with sterile PBS, and their steady-state sterol composition was determined by reverse-phase HPLC analysis, as described in detail elsewhere [117].

PCR and mutation verification

Genomic DNA from SLOS RPE cells was extracted using a proteinase K-based method. Briefly, SLOS RPE cells were scraped and pelleted followed by a 4-h incubation at 55°C in All^{ele}-In-One™ Mouse Tail Direct PCR buffer (Allele Biotechnology, ABP-PP-MT01500). The one-step reaction provided the genomic template that was directly applied for PCR amplification using REDTaq® DNA Polymerase (Sigma-Aldrich, D4309), and MyIQ™ Single Color Real-Time PCR Detection System (Biorad Laboratories, 170–9740). The SLOS patient's *DHCR7* mutations (in the strain of fibroblasts from which the iPSCs were generated) previously had been determined to be compound heterozygous mutations consisting of T93M and IVS8G-C point mutations [28,118]. Primers designed to flank the 2 point mutations were as follows: a) T93M Fwd 5′ – GCGAGCGTCATCTTCCTAC – 3′, T93M Rev 5′ – CAGGATCCATGTCCCAGAC – 3′ (which yields a 296 bp PCR product), and b) IVS8G-C Fwd 5′ – CAGAGGCAGAGCTGGGG – 3′, IVS8G-C Rev 5′-CAGCAGGCGGTAAGGCA – 3′ (which yields a 557 bp PCR product). The PCR products thus obtained were electrophoresed on a 1.5% agarose gel to verify product size, in comparison with a DNA standard mixture (ThermoFisher Scientific, 15,628,019) applied in a separate lane, and visualized using a FOTODYNE FOTO/UV® 21 Transilluminator (FOTODYNE Inc.,USA). PCR products were excised from the gel and extracted using a QIAquick® Gel Extraction Kit (Qiagen, 28,704), per the manufacturer's protocol, then sequenced at Roswell Park Cancer Institute (RPCI) Genomics Shared Resource (Buffalo, NY, USA). The sequence readout from SLOS RPE was compared to the known *DHCR7* sequence (NM_001360) using the ClustalW2 (now Clustal Omega) Multiple Sequence Alignment Program (EMBL-EBI) to verify the presence and identity of point mutations in the SLOS RPE cells [119].

SDS-PAGE, western blot and densitometric analyses

Cells were washed 3 times with modified Hanks' Balanced Salt Solution (HBSS), and lysed with RIPA lysis and extraction buffer (ThermoFisher Scientific, 89,900) supplemented with protease inhibitor cocktail (ThermoFisher Scientific, 78,441) at 1:100 dilution. Protein yield was estimated using a Pierce™ BCA Protein Assay Kit (ThermoFisher Scientific, 23,225). Equal amounts of protein were loaded in each lane on either 12% or 15% SDS-PAGE gels. Upon electrophoresis, western blot analysis of proteins was performed as previously described [12]. In brief, proteins were electrophoretically transferred to low fluorescence PVDF membrane (Bio-Rad Laboratories, 1,620,264) using a semi-dry transfer apparatus (Bio-Rad) [12]. Membranes were blocked for 1 h at room temperature using 5% (w:v) nonfat dry milk in Tris-buffered

saline (TBST; 50 mM Tris-Cl, 150 mM NaCl, 0.1% [v:v] Tween-20 [Sigma Aldrich, 9005–64-5], pH 7.5), and then incubated overnight at 4°C with primary antibodies at 4°C: Rabbit anti-RLBP1 protein (Abcam, ab154898; 1:1000); mouse anti-acetylated tubulin (ThermoFisher Scientific, 32–2700; 1:500); mouse anti-BEST1/bestrophin-1 (Novus Biologicals, NB300-164; 1:1000); mouse anti-KRT8-KRT18/cytokeratin 8/18 (Abcam, ab17139; 1:1000); mouse anti-ubiquitin (Santa Cruz Biotechnology, Inc., scP1A6; 1:500; a generous gift from Dr. Wilma Hoffman, SUNY Buffalo, NY, USA); rabbit anti-MAP1LC3B (Cell Signaling Technology, 2775; 1:1000); mouse anti-SQSTM1 (Abcam, ab56416; 1:1000); rabbit anti-ATG5 (Cell Signaling Technology, 2630; 1:1000); anti-RHO mouse monoclonal antibody (1D4, 1:2000; a generous gift from Dr. Robert Molday, University of British Columbia, Canada); rabbit anti-ACTB (Cell Signaling Technology, 4967; 1:1000). After rinsing the membranes 3 times with TBST, a follow-up incubation was carried out using appropriate host-specific alkaline phosphatase-tagged secondary antibodies (1 h at room temperature). Detection of antibody binding was achieved using chemifluorescent enzyme substrate (GE Healthcare Life Sciences, 45,000,947) and a ChemiDoc™ MP Imaging System (Bio-Rad Laboratories, USA). Semi-quantitative densitometric analysis was performed using ImageLab® 5.0 software (Bio-Rad Laboratories, USA), with band intensities of target antigens normalized to ACTB levels.

Immunohistochemistry and confocal microscopy

Eyes from control and AY9944-treated animals were enucleated (6-h post light onset), fixed in PBS 3.7% (w:v) formaldehyde (prepared from paraformaldehyde; Electron Microscopy Sciences, 30,525–89-4)) on ice for 15 min, and then rinsed in chilled PBS 3 times. Fixed eyes were cryoprotected overnight at 4°C by immersion in 30% (w:v) sucrose (Sigma Aldrich, 57–50-1) in PBS, and then embedded in TissueTek® Optimal Cutting Temperature Compound (Electron Microscopy Sciences, 62,550–01). Cryosections (10-micron thickness) were collected onto glass Gold Seal™ UltraFrost™ microscope slides (Thermo Fisher Scientific, 3063–002), using a cryostat (CM3050S, Leica Microsystems, Buffalo Grove, IL, USA). Tissue cryosections were then treated with dry ice-chilled acetone for 10 min, air-dried, and subjected to brief immersion in PBS containing 100 mM glycine (to block free aldehyde groups), followed by 2 brief rinses in PBS. To block nonspecific binding of secondary antibodies (host origin: donkey or goat), sections were treated with nonimmune (normal) donkey (Sigma Aldrich, D9663) or goat (Sigma Aldrich, G9023) serum (5% [v:v] in TBS, supplemented with 0.2% [v:v] Tween-20, 0.5% [w:v] BSA (Sigma Aldrich, A3059), and 0.5% [w:v] fish skin gelatin (Sigma Aldrich, G7061). Cryosections were then briefly rinsed with TBST, and exposed (overnight at 4°C in a humidified chamber) to primary antibodies (diluted in TBST supplemented with 0.5% [w:v] BSA): rabbit anti-RLBP1 (1:200); mouse anti-TJP1 (Molecular Probes, 339,100; 1:100); mouse anti-RHO (1D4; 1:200); rabbit anti-CTSD (Calbiochem, M16; 1:100). Negative controls consisted of nonimmune IgG (10 μg/ml) (Sigma Aldrich; rabbit: 12–370, mouse: 12–371): from the same host species as that from which the primary antibody was derived. After 3 rinses with TBST, tissue sections were incubated for 45 min at room temperature with secondary IgG from suitable host species, conjugated with Alexa Fluor® 410/488/568/647 (1:500 in antibody diluent; ThermoFisher Scientific, Grand Island, NY). Slides were rinsed with TBS, counterstained with DAPI (4′,6-diamido-2-phenylindole), coverslip mounted using Vectashield® mounting medium (Vector Laboratories, H-1000), and examined with a Leica TCS SPEII DMI4000 scanning laser confocal fluorescence microscope (Leica Microscystems, Buffalo Grove, IL, USA). Images were captured using a 40X or 63X oil immersion (RI-1.518) objective under nominal laser intensity (10%-20% of maximum intensity), arbitrary gain (800–900) and offset (−0.2) values, to optimize the signal-to-noise ratio.

For analysis of autofluorescence, cryosections of formaldehyde-fixed Optimal Cutting Temperature Compound-embedded eyes (see above) from 3-month old-untreated (control) and AY9944-treated rats were mounted, air-dried, hydrated, and coverslipped on glass slides without staining. Maximum z-stack projections (42 x 0.065-μm xy sections) were captured by scanning laser confocal fluorescence microscopy, using 488-nm excitation and emission window set between 500- to 600-nm[120]. Leica software (LAS-AF, version 4.4) functions (thresholding with pixel-oriented segmentation) were employed for quantification of RPE autofluorescent inclusions; pixel intensities were summed and grouped as a function of particle diameter (d) into 3 groups: those with $d < 0.28$ μm; those with $d = 0.28$ to 0.70 μm; and those with $d > 0.70$ μm.

Lysosomal ph measurement

SLOS RPE cells cultured on 96-well plates were utilized for lysosomal pH measurements, using LysoSensor™ Yellow/Blue DND-160 (ThermoFisher Scientific, L7545), a membrane-permeable ratiometric pH-sensitive probe (pKa ~ 4.2), which emits a blue fluorescence in neutral pH environments, but changes to yellow fluorescence in more acidic environments. The procedure employed was essentially as described previously [44]. Culture medium was aspirated from the cells, which were then incubated with LysoSensor™ Yellow/Blue DND-160 (2 μM; ThermoFisher Scientific, L7545), prepared in an isotonic solution containing 105 mM NaCl, 5 mM KCl, 6 mM HEPES-acid, 4 mM HEPES-Na, 5 mM $NaHCO_3$, 60 mM mannitol (Sigma Aldrich, M4125), 5 mM glucose (Sigma Aldrich, G8270), 500 μM $MgCl_2$, and 1.3 mM $CaCl_2$, pH 7.4; 300 mOsm. After a 3-min incubation, cells were rinsed 3 times with the same isotonic solution, followed by treatment with chloroquine (CHQ, as the diphosphate) and pH standards. Lysosomal pH of cells in 'calibration wells' was calibrated against a range of pH values (pH 4.0, 4.5, 5.0, 5.5 and 6.5) by incubation in a solution containing 20 mM MES (2-(N-morpholino)ethanesulfonic acid), 110 mM NaCl, 5 mM KCl, 15 μM monensin (Sigma Aldrich, M5273), and 30 μM nigericin (Sigma Aldrich, N7143). Monensin and nigericin are proton-cation ionophores that render membranes permeable to Na^+ and K^+, respectively. Lysosomal pH values were

expressed as the ratio of the emitted light intensities (measured at 527 nm) with excitation at 340 nm *vs*. 380 nm, using a Fluoroskan Ascent™ FL Microplate Fluorometer and Ascent™ software (ThermoFisher Scientific, Grand Island, NY). Eleven iterations of readings were obtained between 12 to 14 min after removal of the dye, of which reading 3 through 7 were used to determine lysosomal pH. Excitation wavelength readouts from calibrated RPE cells with known pH values were used as standards to plot absolute pH values of cells.

Measurement of CTSD activity

CTSD activity in cultured cells was estimated using an assay based on binding of fluor-tagged pepstatin A (BODIPY-FL Pepstatin-A analog; Invitrogen, P12271), as previously described [43,44]. Briefly, SLOS RPE cells were cultured to confluence in black-walled, clear-bottomed 96-well plates. Cells were incubated in Mg^{2+}-free isotonic solution for an hour, followed by a 30-min dark incubation with 10 μM Bodipy FL-labelled Pepstatin-A (Molecular Probes®) at 37°C. CTSD active site levels were evaluated as an autofluorescence-corrected fluorescence readout (excitation/emission ratio: λ_{ex} = 340 nm; λ_{em} = 380 nm), obtained using the aforementioned fluorescence microplate reader.

A2E and bisretinoid measurements

Eyes (n = 4 per group/treatment) from untreated and AY9944-treated rats were harvested, flash frozen in liquid nitrogen, and stored at −80°C until ready for analysis. Analysis of A2E, related bisretinoids, and all-*trans* retinaldehyde was performed by ultra-performance liquid chromatography-mass spectrometry (UPLC-MS) as described in detail elsewhere [121]. In brief, after extraction in the presence of chloroform and methanol, analysis was performed on a Waters ACQUITY UPLC System (Waters/Millipore) that was coupled on-line with a Waters SQD single quadrupole mass spectrometer (electrospray ion multi-mode ionization, ESCi) and both photodiode array (PDA) eλ and fluorescence (FLR, Waters, Milford, MA, USA) detectors. For elution, a Waters XBridge™ C18 reversed phase column (2.5 μm, 3 × 50 mm) was used with a mobile phase of acetonitrile/methanol (1:1) in water. Peak area was determined from chromatograms using Waters Empower software and molar quantity per eye was determined using calibration curves constructed from known concentrations of synthesized standards and by normalizing to the ratio of the HPLC injection volume (10 μl) *vs*. total extract volume. These data were then correlated with the qualitative and quantitative autofluorescence data obtained from the scanning laser confocal fluorescence microscopy analysis of ocular cryosections (see above, and *Results*).

Transduction with bacmam RFP-GFP-LC3B construct to detect autophagic flux

Formation and maturation of autophagosomes was monitored in control and SLOS RPE cells by transient transduction utilizing a Premo™ Autophagy Tandem Sensor RFP-GFP-LC3B Kit (ThermoFisher Scientific, P36239) as described by the manufacturer. Briefly, RPE cells cultured on RINZL coverslips were incubated with 30 particles/cell of the BacMam reagent containing the RFP-GFP-LC3B construct (n = 3), for 24 h in the cell culture incubator as described above. Transduced control RPE cells (n = 3) were incubated in 150 μM CHQ for 8 h. The cells were rinsed in 1X PBS followed by 4% buffered paraformaldehyde fixation for 10 min. Fixed coverslips were then rinsed, and counterstained with DAPI. Coverslips were mounted using Vectashield® mounting medium, and high magnification confocal fluorescence microscopy images were obtained as described in *Section 4.7*. Transduced cells were selected for microscopy based on RFP signal alone and RFP/GFP signals were subsequently captured. The number of GFP- and RFP-positive puncta were manually counted (n = 100/group/treatment), and the GFP/RFP ratio provided an estimate of the percentage of unacidified (immature) phagosomes under each condition.

Bovine rod outer segment (ROS) phagocytosis and degradation assay

ROS prepared under dim red light from dark-adapted bovine retinas was obtained commercially (InVision BioResources, 98,740). Phagocytosis assay was performed as described in detail elsewhere [122]. Briefly, control and SLOS RPE cells were maintained at confluence in 6-well plates for 2 to 3 months. Cultures were then treated for 2 h (at 37°C) with aliquots of ROS (suspended in culture medium), at a final calculated ratio of 5 ROS particles/cell, followed by 3x washes of all cultures with fresh medium to remove any nonphagocytosed ROS. Triplicate cultures were harvested at 2 h, to verify and quantify outer segment phagocytosis. The remaining 3 wells were then incubated for an additional 48 h (at 37°C), before lysing the cells in RIPA buffer supplemented with protease inhibitors. The protein concentration in the lysates was determined (micro-BCA assay; Pierce), followed by immunoblot analysis (see above), utilizing antibodies against RHO (1D4 mouse monoclonal) and ACTB (rabbit monoclonal; [Cell Signaling Technology, 4970S]).

Measurement of transepithelial electrical resistance (TEER)

Control and SLOS RPE cells were seeded in triplicate on 12-well Transwell® inserts (Millipore, MCRP12H48) coated with iMatrix-511®, at a density of ~ 3.2 x 10^4 cells/Transwell®. The cells were cultured using the strategy described above. To monitor the establishment of an electrically tight epithelial monolayer, TEER measurements were made every week using an epithelial volt-ohm meter (E-VOM^2, World Precision Instruments, Sarasota, FL, USA). Three measurements were obtained from each well, and an average TEER value (expressed as $\Omega^{*}cm^2$) was calculated as the product of the area of the insert and the epithelial resistance measurement (obtained by subtracting the TEER measurements obtained from a blank insert from total TEER measurement) [123].

RNA extraction, cdna synthesis and qpcr

Cultured control and SLOS RPE cells (n = 3 each) were dislodged using accutase treatment and pelleted by centrifugation. Cells were lysed using an RNeasy® Plus Mini Kit (Qiagen, 74,134) per manufacturer's instructions; lysates were passed through a QIAshredder column (Qiagen, 79,654) to ensure homogenization, followed by genomic DNA digestion using gDNA eliminator spin columns. RNA was purified using RNeasy® columns, and quantified. Samples of RNA (150 ng each) were taken for cDNA preparation, using an AffinityScript® QPCR cDNA synthesis kit (Agilent Technologies, 600,559) per the manufacturer's instruction. cDNA was subjected to qPCR using iQ™ SYBR® Green RT mix (Bio-Rad, 1,708,880). The primer sequence for RPE-specific/housekeeping transcript targets were as follows: *RPE65*: Fwd 5′ CTGTTCAAGTTCCTTTCTTCATGG 3′, Rev 5′ GTCAGCAATATGAAGCCAACC 3′; *MERTK*: Fwd 5′ CTTCGTGCTGGGCTTCTAC 3′, Rev 5′ TTGCTCGTCCTTGCCTTC 3′; *MITF*: Fwd 5′ CCAGTATGACATCACGCATCT 3′, Rev 5′ ACTCACGGGCACTCTCT 3′; and, *ACTB*: Fwd 5′ GTCCCCCAACTTGAGATGTATG 3′, Rev 5′ AAGTCAGTGTACAGGTAAGCC 3′. A HEK293S cDNA library (a generous gift from Zahra Fayazi, University at Buffalo, NY, USA) was used as a negative control for qPCR analysis of RPE-specific transcript targets in control and SLOS RPE. The normalized expression ratio [$2^{(-\Delta\Delta Ct)}$] (normalized to *ACTB)* for the target transcripts was calculated using the Livak method [34].

Statistical analysis of quantitative data

One-way ANOVA (analysis of variance) was performed to test for statistical significance of differences between quantitative values derived from specific experimental protocols, using GraphPad® software package. One-ANOVA determined statistical significance, if any, between three or more categorical groups. Further, the Welch's unpaired t test (which assumes unequal variances between individual groups of data) was employed as post-hoc test. In either case, a significance threshold of $P < 0.05$ was applied.

Abbreviations

3-MA	3-methyladenine;
7DHC	7-dehydrocholesterol;
ACTB	actin beta;
ATG5	autophagy related 5;
BCS	bovine calf serum;
Chol	cholesterol;
CHQ	chloroquine;
DHCR7	7-dehydrocholesterol reductase;
DLS	delipidated serum;
ERG	electroretinography/electroretinographic;
ESC	embryonic stem cell;
GFP	green fluorescent protein;
HPLC	high-pressure liquid chromatography;
iPSC	induced pluripotent stem cell;
LAP	LC3-associated phagocytosis;
LDL	low-density lipoprotein;
MAP1LC3B	microtubule associated protein 1 light chain 3 beta;
MERTK	MER proto-oncogene tyrosine kinase;
MITF	melanogenesis associated transcription factor;
NPC1	NPC intracellular cholesterol transporter 1;
PE	phosphatidylethanolamine;
qPCR	quantitative polymerase chain reaction;
RAB7	RAB7, member RAS oncogene family;
RFP	red fluorescent protein;
RFU	relative fluorescence unit;
RHO	rhodopsin;
RLBP1	retinaldehyde binding protein 1;
ROS	rod outer segment;
RPE	retinal pigment epithelium;
RPE65	RPE65, retinoid isomerohydrolase;
SLOS:	Smith-Lemli-Opitz syndrome;
TEER	transepithelial electrical resistance;
TJP1	tight junction protein 1;
TUBA/α-tubulin	tubulin alpha;
UPLC-MS	ultra-performance liquid chromatography-mass spectrometry

Acknowledgments

We gratefully acknowledge the technical assistance of Meerim Choi, Cheryl Dann, Rebecca Benz, and Dr. Zahra Fayazi in the course of this study. We thank: Drs. Kevin Francis, Christopher Wassif and Forbes D. Porter (NIH/NICHD, Bethesda, MD, USA) for the generous gift of SLOS patient-derived iPSCs, as well as eyes from the T93M/Δ3-5 genetic murine SLOS model; Dr. Lincoln V. Johnson (Institute for Collaborative Technologies and Center for the Study of Macular Degeneration, UCSB, Santa Barbara, CA, USA) for the normal human ESC-derived RPE cells (nhRPE); Drs Barbara Corneo and Sally Temple (Neural Stem Cell Institute, Rensselaer, NY, USA) for differentiation of the SLOS-derived iPSCs to SLOS RPE cells; and Dr. Barbara Corneo (Columbia University Stem Cell Core Facility) for differentiation of DYS0100 normal iPSCs to RPE cells. Portions of this work have been presented in preliminary form at Annual Meetings of the Association for Research in Vision and Ophthalmology (ARVO; 2015-2017) and the 2016 Biennial Meeting of the International Society for Eye Research (ISER). The opinions expressed herein do not necessarily reflect those of the Veterans Administration, the National Institutes of Health, or the U.S. Government.

Disclosure statement

No potential conflict of interest was reported by the authors.

Funding

Supported, in part, by U.S.P.H.S. (NIH) grants R01 EY007361 (SJF), 1 UL1 TR001412 (to SUNY-University at Buffalo (SJF)), R01 EY012951 (JRS), R01 EY013434 and R01 EY015537 (CHM); by an Unrestricted Grant from Research to Prevent Blindness to the Department of Ophthalmology, SUNY-University at Buffalo (SJF); and by facilities and resources provided by the VA Western NY Healthcare System (SJF). SJF is the recipient of a Research Career Scientist Award (RCSA) from the Department of Veterans Affairs, BLR&D Service. SRR was the recipient of 2 Fight for Sight Summer Student Fellowships. SJF and CHM were participants in the Lab Exchange Program of the International Society for Eye Research (ISER), which supported a travel award for NMG to attend the 2017 ISER Biennial meeting (Tokyo, Japan), at which some of the results obtained in the current study were presented; National Eye Institute/NIH [R01 EY007361]; NEI/NIH [R01 EY012951]; National Eye Institute/NIH [R01 EY013434]; Fight for Sight Student Summer Research Grant [None]; National Center for Advancing Translational Sciences/NIH [UL1 TR001412]; Research to Prevent Blindness Unrestricted Grant [None]; NEI/NIH [R01 EY015537].

References

[1] Smith DW, Lemli L, Opitz JM. A newly recognized syndrome of multiple congenital anomalies. J Pediatr. 1964 Feb;64:210–217. PubMed PMID: 14119520

[2] Bloch K. Sterol structure and function. Steroids. 1989 Mar-May;53 (3–5):261–270. PubMed PMID: 2799845

[3] Yu H, Lee MH, Starck L, et al. Spectrum of Delta(7)-dehydrocholesterol reductase mutations in patients with the Smith-Lemli-Opitz (RSH) syndrome. Hum Mol Genet. 2000 May 22;9 (9):1385–1391. PubMed PMID: 10814720

[4] Honda A, Tint GS, Salen G, et al. Defective conversion of 7-dehydrocholesterol to cholesterol in cultured skin fibroblasts from Smith-Lemli-Opitz syndrome homozygotes. J Lipid Res. 1995 Jul;36(7):1595–1601. PubMed PMID: 7595082

[5] Shefer S, Salen G, Batta AK, et al. Markedly inhibited 7-dehydrocholesterol-delta 7-reductase activity in liver microsomes from Smith-Lemli-Opitz homozygotes. J Clin Invest. 1995 Oct;96 (4):1779–1785. PubMed PMID: 7560069; PubMed Central PMCID: PMC185814.

[6] Xu L, Korade Z, Rosado DA Jr. et al. An oxysterol biomarker for 7-dehydrocholesterol oxidation in cell/mouse models for Smith-Lemli-Opitz syndrome. J Lipid Res. 2011 Jun;52(6):1222–1233..PubMed PMID: 21402677; PubMed Central PMCID: PMC3090243

[7] Xu L, Korade Z, Porter NA. Oxysterols from free radical chain oxidation of 7-dehydrocholesterol: product and mechanistic studies. J Am Chem Soc. 2010 Feb 24;132(7):2222–2232.. PubMed PMID: 20121089; PubMed Central PMCID: PMC2839323.

[8] Xu L, Sheflin LG, Porter NA, et al. 7-Dehydrocholesterol-derived oxysterols and retinal degeneration in a rat model of Smith-Lemli-Opitz syndrome. Biochim Biophys Acta. 2012 Jun;1821(6):877–883. PubMed PMID: 22425966; PubMed Central PMCID: PMC3340457.

[9] Lin AE, Ardinger HH, Ardinger RH Jr., et al. Cardiovascular malformations in Smith-Lemli-Opitz syndrome. Am J Med Genet. 1997 Jan 31;68(3):270–278. PubMed PMID: 9024558

[10] Witsch-Baumgartner M, Fitzky BU, Ogorelkova M, et al. Mutational spectrum in the Delta7-sterol reductase gene and genotype-phenotype correlation in 84 patients with Smith-Lemli-Opitz syndrome. Am J Hum Genet. 2000 Feb;66(2):402–412. PubMed PMID: 10677299; PubMed Central PMCID: PMC1288092.

[11] Kretzer FL, Hittner HM, Mehta RS. Ocular manifestations of the Smith-Lemli-Opitz syndrome. Arch Ophthalmol. 1981 Nov;99 (11):2000–2006. PubMed PMID: 7295150

[12] Garry D, Hansen RM, Moskowitz A, et al. Cone ERG responses in patients with Smith-Lemli-Opitz Syndrome (SLOS). Doc Ophthalmol. 2010 Oct;121(2):85–91. PubMed PMID: 20440536; PubMed Central PMCID: PMC2935499.

[13] Fliesler SJ, Peachey NS, Richards MJ, et al. Retinal degeneration in a rodent model of Smith-Lemli-Opitz syndrome: electrophysiologic, biochemical, and morphologic features. Arch Ophthalmol. 2004 Aug;122(8):1190–1200. PubMed PMID: 15302661; PubMed Central PMCID: PMC2865831.

[14] Tu C, Li J, Jiang X, et al. Ion-current-based proteomic profiling of the retina in a rat model of Smith-Lemli-Opitz syndrome. Mol Cell Proteomics. 2013 Dec;12(12):3583–3598. PubMed PMID: 23979708; PubMed Central PMCID: PMC3861709.

[15] Boesze-Battaglia K, Damek-Poprawa M, Mitchell DC, et al. Alteration of retinal rod outer segment membrane fluidity in a rat model of Smith-Lemli-Opitz syndrome. J Lipid Res. 2008 Jul;49(7):1488–1499. PubMed PMID: 18344409; PubMed Central PMCID: PMC2431111.

[16] Ford DA, Monda JK, Brush RS, et al. Lipidomic analysis of the retina in a rat model of Smith-Lemli-Opitz syndrome: alterations in docosahexaenoic acid content of phospholipid molecular species. J Neurochem. 2008 May;105(3):1032–1047. PubMed PMID: 18182048; PubMed Central PMCID: PMC2721972.

[17] Fliesler SJ, Richards MJ, Miller C, et al. Marked alteration of sterol metabolism and composition without compromising retinal development or function. Invest Ophthalmol Vis Sci. 1999 Jul;40 (8):1792–1801. PubMed PMID: 10393050

[18] Fliesler SJ, Peachey NS, Herron J, et al. Prevention of retinal degeneration in a rat model of Smith-Lemli-Opitz Syndrome. Sci Rep. 2018 Jan 19;8(1):1286. 10.1038/s41598-018-19592-8. PubMed PMID: 29352199; PubMed Central PMCID: PMC5775248

[19] Frost LS, Mitchell CH, Boesze-Battaglia K. Autophagy in the eye: implications for ocular cell health. Exp Eye Res. 2014 Jul;124:56–66. PubMed PMID: 24810222; PubMed Central PMCID: PMC4156154.

[20] Ferguson TA, Green DR. Autophagy and phagocytosis converge for better vision. Autophagy. 2014 Jan;10(1):165–167..PubMed PMID: 24220227; PubMed Central PMCID: PMC4028322

[21] Young RW, Bok D. Participation of the retinal pigment epithelium in the rod outer segment renewal process. J Cell Biol. 1969 Aug;42(2):392–403. PubMed PMID: 5792328; PubMed Central PMCID: PMC2107669

[22] Kellner U, Kellner S, Weinitz S. Chloroquine retinopathy: lipofuscin- and melanin-related fundus autofluorescence, optical coherence tomography and multifocal electroretinography. Doc Ophthalmol. 2008 Mar;116(2):119–127..PubMed PMID: 18080820

[23] Yoon YH, Cho KS, Hwang JJ, et al. Induction of lysosomal dilatation, arrested autophagy, and cell death by chloroquine in cultured ARPE-19 cells. Invest Ophthalmol Vis Sci. 2010 Nov;51 (11):6030–6037. PubMed PMID: 20574031.

[24] Matsumura M, Ohkuma M, Tsukahara I. Experimental chloroquine retinopathy. Ophthalmic Res. 1986;18(3):172–179. PubMed PMID: 3018650

[25] Mahon GJ, Anderson HR, Gardiner TA, et al. Chloroquine causes lysosomal dysfunction in neural retina and RPE: implications for retinopathy. Curr Eye Res. 2004 Apr;28(4):277–284. PubMed PMID: 15259297

[26] Kim JY, Zhao H, Martinez J, et al. Noncanonical autophagy promotes the visual cycle. Cell. 2013 Jul 18;154(2):365–376. PubMed PMID: 23870125; PubMed Central PMCID: PMC3744125.

[27] Gal A, Li Y, Thompson DA, et al. Mutations in MERTK, the human orthologue of the RCS rat retinal dystrophy gene, cause retinitis pigmentosa. Nat Genet. 2000 Nov;26(3):270–271. PubMed PMID: 11062461.

[28] Francis KR, Ton AN, Xin Y, et al. Modeling Smith-Lemli-Opitz syndrome with induced pluripotent stem cells reveals a causal role for Wnt/beta-catenin defects in neuronal cholesterol synthesis phenotypes. Nat Med. 2016 Apr;22(4):388–396. PubMed PMID: 26998835; PubMed Central PMCID: PMC4823163.

[29] Maminishkis A, Chen S, Jalickee S, et al. Confluent monolayers of cultured human fetal retinal pigment epithelium exhibit morphology and physiology of native tissue. Invest Ophthalmol Vis Sci. 2006 Aug;47(8):3612–3624. PubMed PMID: 16877436; PubMed Central PMCID: PMC1904392.

[30] Saari JC, Nawrot M, Kennedy BN, et al. Visual cycle impairment in cellular retinaldehyde binding protein (CRALBP) knockout mice results in delayed dark adaptation. Neuron. 2001 Mar;29 (3):739–748. PubMed PMID: 11301032

[31] Toops KA, Tan LX, Jiang Z, et al. Cholesterol-mediated activation of acid sphingomyelinase disrupts autophagy in the retinal pigment epithelium. Mol Biol Cell. 2015 Jan 01;26(1):1–14. PubMed PMID: 25378587; PubMed Central PMCID: PMC4279221.

[32] Xie R, Nguyen S, McKeehan WL, et al. Acetylated microtubules are required for fusion of autophagosomes with lysosomes. BMC Cell Biol. 2010 Nov 22;11:89.. PubMed PMID: 21092184; PubMed Central PMCID: PMC2995476.

[33] Marmorstein AD, Marmorstein LY, Rayborn M, et al. Bestrophin, the product of the Best vitelliform macular dystrophy gene (VMD2), localizes to the basolateral plasma membrane of the retinal pigment epithelium. Proc Natl Acad Sci U S A. 2000 Nov 7;97(23):12758–12763. PubMed PMID: 11050159; PubMed Central PMCID: PMC18837.

[34] Livak KJ, Schmittgen TD. Analysis of relative gene expression data using real-time quantitative PCR and the 2(-Delta Delta C(T))

Method. Methods. 2001 Dec;25(4):402–408..PubMed PMID: 11846609
[35] Pfeffer BA, Becerra SP, Borst DE, et al. Expression of transthyretin and retinol binding protein mRNAs and secretion of transthyretin by cultured monkey retinal pigment epithelium. Mol Vis. 2004 Jan;14(10):23–30. PubMed PMID: 14737066
[36] Pfeffer BA. Improved methodology for cell culture of human and monkey retinal pigment epithelium. Prog Retin Res. 1991;10:251–291..PubMed PMID: WOS:A1991HK14200009; English
[37] Yu H, Tint GS, Salen G, et al. Detection of a common mutation in the RSH or Smith-Lemli-Opitz syndrome by a PCR-RFLP assay: IVS8-G–>C is found in over sixty percent of US propositi. Am J Med Genet. 2000 Feb 14;90(4):347–350. PubMed PMID: 10710236
[38] Krakowiak PA, Nwokoro NA, Wassif CA, et al. Mutation analysis and description of sixteen RSH/Smith-Lemli-Opitz syndrome patients: polymerase chain reaction-based assays to simplify genotyping. Am J Med Genet. 2000 Sep 18;94(3):214–227. PubMed PMID: 10995508
[39] Bjorkoy G, Lamark T, Brech A, et al. p62/SQSTM1 forms protein aggregates degraded by autophagy and has a protective effect on huntingtin-induced cell death. J Cell Biol. 2005 Nov 21;171(4):603–614. PubMed PMID: 16286508; PubMed Central PMCID: PMC2171557.
[40] Wang L, Cano M, Handa JT. p62 provides dual cytoprotection against oxidative stress in the retinal pigment epithelium. Biochim Biophys Acta. 2014 Jul;1843(7):1248–1258..PubMed PMID: 24667411; PubMed Central PMCID: PMC4019388
[41] Miettinen TP, Bjorklund M. Mevalonate pathway regulates cell size homeostasis and proteostasis through autophagy. Cell Rep. 2015 Dec 22;13(11):2610–2620.. PubMed PMID: 26686643; PubMed Central PMCID: PMC4709259.
[42] Tricarico PM, Crovella S, Celsi F. Mevalonate pathway blockade, mitochondrial dysfunction and autophagy: a possible link. Int J Mol Sci. 2015 Jul 15;16(7):16067–16084.. PubMed PMID: 26184189; PubMed Central PMCID: PMC4519939.
[43] Coffey EE, Beckel JM, Laties AM, et al. Lysosomal alkalization and dysfunction in human fibroblasts with the Alzheimer's disease-linked presenilin 1 A246E mutation can be reversed with cAMP. Neuroscience. 2014 Mar 28;263:111–124.. PubMed PMID: 24418614; PubMed Central PMCID: PMC4028113.
[44] Guha S, Coffey EE, Lu W, et al. Approaches for detecting lysosomal alkalinization and impaired degradation in fresh and cultured RPE cells: evidence for a role in retinal degenerations. Exp Eye Res. 2014 Sep;126:68–76. PubMed PMID: 25152362; PubMed Central PMCID: PMC4143779.
[45] Barth S, Glick D, Macleod KF. Autophagy: assays and artifacts. J Pathol. 2010 Jun;221(2):117–124..PubMed PMID: 20225337; PubMed Central PMCID: PMC2989884
[46] Tanida I, Ueno T, Kominami E. LC3 and Autophagy. Methods Mol Biol. 2008;445:77–88..PubMed PMID: 18425443
[47] Pankiv S, Clausen TH, Lamark T, et al. p62/SQSTM1 binds directly to Atg8/LC3 to facilitate degradation of ubiquitinated protein aggregates by autophagy. J Biol Chem. 2007 Aug 17;282(33):24131–24145. PubMed PMID: 17580304.
[48] Gottlieb RA, Andres AM, Sin J, et al. Untangling autophagy measurements: all fluxed up. Circ Res. 2015 Jan 30;116(3):504–514.. PubMed PMID: 25634973; PubMed Central PMCID: PMC4313387.
[49] Klionsky DJ, Abdelmohsen K, Abe A, et al. Guidelines for the use and interpretation of assays for monitoring autophagy (3rd edition). Autophagy. 2016;12(1):1–222..PubMed PMID: 26799652; PubMed Central PMCID: PMC4835977
[50] Sahani MH, Itakura E, Mizushima N. Expression of the autophagy substrate SQSTM1/p62 is restored during prolonged starvation depending on transcriptional upregulation and autophagy-derived amino acids. Autophagy. 2014 Mar;10(3):431–441..PubMed PMID: 24394643; PubMed Central PMCID: PMC4077882
[51] Hanada T, Noda NN, Satomi Y, et al. The Atg12-Atg5 conjugate has a novel E3-like activity for protein lipidation in autophagy. J Biol Chem. 2007 Dec 28;282(52):37298–37302. PubMed PMID: 17986448.
[52] Kim M, Sandford E, Gatica D, et al. Mutation in ATG5 reduces autophagy and leads to ataxia with developmental delay. Elife. 2016 Jan;26:5. PubMed PMID: 26812546; PubMed Central PMCID: PMC4786408.
[53] Mizushima N, Yoshimori T, Levine B. Methods in mammalian autophagy research. Cell. 2010 Feb 5;140(3):313–326.. PubMed PMID: 20144757; PubMed Central PMCID: PMC2852113.
[54] Deguchi J, Yamamoto A, Yoshimori T, et al. Acidification of phagosomes and degradation of rod outer segments in rat retinal pigment epithelium. Invest Ophthalmol Vis Sci. 1994 Feb;35(2):568–579. PubMed PMID: 8113008
[55] Bosch E, Horwitz J, Bok D. Phagocytosis of outer segments by retinal pigment epithelium: phagosome-lysosome interaction. J Histochem Cytochem. 1993 Feb;41(2):253–263..PubMed PMID: 8419462
[56] Wavre-Shapton ST, Meschede IP, Seabra MC, et al. Phagosome maturation during endosome interaction revealed by partial rhodopsin processing in retinal pigment epithelium. J Cell Sci. 2014 Sep 01;127(Pt 17):3852–3861. PubMed PMID: 25074813; PubMed Central PMCID: PMC4150067.
[57] Esteve-Rudd J, Lopes VS, Jiang M, et al. In vivo and in vitro monitoring of phagosome maturation in retinal pigment epithelium cells. Adv Exp Med Biol. 2014;801:85–90..PubMed PMID: 24664684
[58] Seglen PO, Gordon PB. 3-Methyladenine: specific inhibitor of autophagic/lysosomal protein degradation in isolated rat hepatocytes. Proc Natl Acad Sci U S A. 1982 Mar;79(6):1889–1892. PubMed PMID: 6952238; PubMed Central PMCID: PMC346086
[59] Fliesler SJ. Antioxidants: the missing key to improved therapeutic intervention in Smith-Lemli-Opitz Syndrome? Hereditary Genet. 2013 Dec 1;2(2):119.. PubMed PMID: 24533230; PubMed Central PMCID: PMC3925008.
[60] Fliesler SJ. Retinal degeneration and cholesterol deficiency [Book Chaper]. Handbook Nutrition, Diet Eye. 2014;1:287–297.
[61] Liu J, Itagaki Y, Ben-Shabat S, et al. The biosynthesis of A2E, a fluorophore of aging retina, involves the formation of the precursor, A2-PE, in the photoreceptor outer segment membrane. J Biol Chem. 2000 Sep 22;275(38):29354–29360. PubMed PMID: 10887199.
[62] Sparrow JR, Boulton M. RPE lipofuscin and its role in retinal pathobiology. Exp Eye Res. 2005 May;80(5):595–606..PubMed PMID: 15862166
[63] Crouch RK, Koutalos Y, Kono M, et al. A2E and Lipofuscin. Prog Mol Biol Transl Sci. 2015;134:449–463..PubMed PMID: 26310170
[64] LaVail MM. Outer segment disc shedding and phagocytosis in the outer retina. Trans Ophthalmol Soc U K. 1983;103(Pt 4):397–404. PubMed PMID: 6380008
[65] Correa-Cerro LS, Wassif CA, Kratz L, et al. Development and characterization of a hypomorphic Smith-Lemli-Opitz syndrome mouse model and efficacy of simvastatin therapy. Hum Mol Genet. 2006 Mar 15;15;(6):839–851. PubMed PMID: 16446309. DOI:10.1093/hmg/ddl003.
[66] Marcos J, Shackleton CH, Buddhikot MM, et al. Cholesterol biosynthesis from birth to adulthood in a mouse model for 7-dehydrosterol reductase deficiency (Smith-Lemli-Opitz syndrome). Steroids. 2007 Oct;72(11–12):802–808. PubMed PMID: 17714750; PubMed Central PMCID: PMC2911235.
[67] Caldwell RB, McLaughlin BJ. Freeze-fracture study of filipin binding in photoreceptor outer segments and pigment epithelium of dystrophic and normal retinas. J Comp Neurol. 1985 Jun 22;236(4):523–537.. PubMed PMID: 4056101.
[68] Punnonen EL, Pihakaski K, Mattila K, et al. Intramembrane particles and filipin labelling on the membranes of autophagic vacuoles and lysosomes in mouse liver. Cell Tissue Res. 1989 Nov;258(2):269–276. PubMed PMID: 2582478
[69] Brandstaetter H, Kishi-Itakura C, Tumbarello DA, et al. Loss of functional MYO1C/myosin 1c, a motor protein involved in lipid raft trafficking, disrupts autophagosome-lysosome fusion.

Autophagy. 2014;10(12):2310–2323..PubMed PMID: 25551774; PubMed Central PMCID: PMC4502697

[70] Amer AO, Byrne BG, Swanson MS. Macrophages rapidly transfer pathogens from lipid raft vacuoles to autophagosomes. Autophagy. 2005 Apr;1(1):53–58. PubMed PMID: 16874021; PubMed Central PMCID: PMC1584280

[71] Koga H, Kaushik S, Cuervo AM. Altered lipid content inhibits autophagic vesicular fusion. FASEB J. 2010 Aug;24(8):3052–3065..PubMed PMID: 20375270; PubMed Central PMCID: PMC2909278

[72] Rai A, Pathak D, Thakur S, et al. Dynein clusters into lipid microdomains on phagosomes to drive rapid transport toward lysosomes. Cell. 2016 Feb 11;164(4):722–734. PubMed PMID: 26853472; PubMed Central PMCID: PMC4752818.

[73] Wijdeven RH, Janssen H, Nahidiazar L, et al. Cholesterol and ORP1L-mediated ER contact sites control autophagosome transport and fusion with the endocytic pathway. Nat Commun. 2016 Jun 10;7:11808.. PubMed PMID: 27283760; PubMed Central PMCID: PMC4906411.

[74] Chang S, Ren G, Steiner RD, et al. Elevated autophagy and mitochondrial dysfunction in the Smith-Lemli-Opitz Syndrome. Mol Genet Metab Rep. 2014;1:431–442..PubMed PMID: 25405082; PubMed Central PMCID: PMC4231544

[75] Fong JT, Kells RM, Gumpert AM, et al. Internalized gap junctions are degraded by autophagy. Autophagy. 2012 May 01;8(5):794–811. PubMed PMID: 22635056; PubMed Central PMCID: PMC3378421.

[76] Carette D, Gilleron J, Denizot JP, et al. New cellular mechanisms of gap junction degradation and recycling. Biol Cell. 2015 Jul;107(7):218–231. PubMed PMID: 25818265.

[77] Ma JH, Wang JJ, Li J, et al. The role of IRE-XBP1 pathway in regulation of retinal pigment epithelium tight junctions. Invest Ophthalmol Vis Sci. 2016 Oct 1;57(13):5244–5252. PubMed PMID: 27701635; PubMed Central PMCID: PMC5054729.

[78] Gordiyenko N, Campos M, Lee JW, et al. RPE cells internalize low-density lipoprotein (LDL) and oxidized LDL (oxLDL) in large quantities in vitro and in vivo. Invest Ophthalmol Vis Sci. 2004 Aug;45(8):2822–2829. PubMed PMID: 15277509.

[79] Tserentsoodol N, Sztein J, Campos M, et al. Uptake of cholesterol by the retina occurs primarily via a low density lipoprotein receptor-mediated process. Mol Vis. 2006 Oct;27(12):1306–1318. PubMed PMID: 17110914

[80] Claudepierre T, Paques M, Simonutti M, et al. Lack of Niemann-Pick type C1 induces age-related degeneration in the mouse retina. Mol Cell Neurosci. 2010 Jan;43(1):164–176. PubMed PMID: 19883762.

[81] Levin R, Grinstein S, Canton J. The life cycle of phagosomes: formation, maturation, and resolution. Immunol Rev. 2016 Sep;273(1):156–179..PubMed PMID: 27558334

[82] Feng Y, He D, Yao Z, et al. The machinery of macroautophagy. Cell Res. 2014 Jan;24(1):24–41. PubMed PMID: 24366339; PubMed Central PMCID: PMC3879710.

[83] Wong E, Cuervo AM. Autophagy gone awry in neurodegenerative diseases. Nat Neurosci. 2010 Jul;13(7):805–811..PubMed PMID: 20581817; PubMed Central PMCID: PMC4038747

[84] Sinha D, Valapala M, Shang P, et al. Lysosomes: regulators of autophagy in the retinal pigmented epithelium. Exp Eye Res. 2016 Mar;144:46–53. PubMed PMID: 26321509; PubMed Central PMCID: PMC4698066.

[85] Ferrington DA, Sinha D, Kaarniranta K. Defects in retinal pigment epithelial cell proteolysis and the pathology associated with age-related macular degeneration. Prog Retin Eye Res. 2016 Mar;51:69–89. PubMed PMID: 26344735; PubMed Central PMCID: PMC4769684.

[86] Lavandero S, Chiong M, Rothermel BA, et al. Autophagy in cardiovascular biology. J Clin Invest. 2015 Jan;125(1):55–64. PubMed PMID: 25654551; PubMed Central PMCID: PMC4382263.

[87] Vieira OV, Botelho RJ, Grinstein S. Phagosome maturation: aging gracefully. Biochem J. 2002 Sep 15;366(Pt 3):689–704.. PubMed PMID: 12061891; PubMed Central PMCID: PMC1222826.

[88] Terman A, Kurz T, Navratil M, et al. Mitochondrial turnover and aging of long-lived postmitotic cells: the mitochondrial-lysosomal axis theory of aging. Antioxid Redox Signal. 2010 Apr;12(4):503–535. PubMed PMID: 19650712; PubMed Central PMCID: PMC2861545.

[89] Cuervo AM, Wong E. Chaperone-mediated autophagy: roles in disease and aging. Cell Res. 2014 Jan;24(1):92–104..PubMed PMID: 24281265; PubMed Central PMCID: PMC3879702

[90] Mitter SK, Song C, Qi X, et al. Dysregulated autophagy in the RPE is associated with increased susceptibility to oxidative stress and AMD. Autophagy. 2014;10(11):1989–2005..PubMed PMID: 25484094; PubMed Central PMCID: PMC4502658

[91] Sparrow JR, Yamamoto K. The bisretinoids of RPE lipofuscin: a complex mixture. Adv Exp Med Biol. 2012;723:761–767..PubMed PMID: 22183404

[92] Ng KP, Gugiu B, Renganathan K, et al. Retinal pigment epithelium lipofuscin proteomics. Mol Cell Proteomics. 2008 Jul;7(7):1397–1405. PubMed PMID: 18436525; PubMed Central PMCID: PMC2493379.

[93] Lakkaraju A, Finnemann SC, Rodriguez-Boulan E. The lipofuscin fluorophore A2E perturbs cholesterol metabolism in retinal pigment epithelial cells. Proc Natl Acad Sci U S A. 2007 Jun 26;104(26):11026–11031.. PubMed PMID: 17578916; PubMed Central PMCID: PMC1904145.

[94] Nixon RA. The role of autophagy in neurodegenerative disease. Nat Med. 2013 Aug;19(8):983–997..PubMed PMID: 23921753

[95] Saadat KA, Murakami Y, Tan X, et al. Inhibition of autophagy induces retinal pigment epithelial cell damage by the lipofuscin fluorophore A2E. FEBS Open Bio. 2014;4:1007–1014..PubMed PMID: 25473597; PubMed Central PMCID: PMC4250541

[96] Lei L, Tzekov R, Li H, et al. Inhibition or stimulation of autophagy affects early formation of lipofuscin-like autofluorescence in the retinal pigment epithelium cell. Int J Mol Sci. 2017 Mar 29;18(4). PubMed PMID: 28353645; PubMed Central PMCID: PMC5412314. DOI:10.3390/ijms18040728.

[97] Simons K, Ehehalt R. Cholesterol, lipid rafts, and disease. J Clin Invest. 2002 Sep;110(5):597–603..PubMed PMID: 12208858; PubMed Central PMCID: PMC151114

[98] Mayor S, Rao M. Rafts: scale-dependent, active lipid organization at the cell surface. Traffic. 2004 Apr;5(4):231–240..PubMed PMID: 15030564

[99] Sarkar S, Carroll B, Buganim Y, et al. Impaired autophagy in the lipid-storage disorder Niemann-Pick type C1 disease. Cell Rep. 2013 Dec 12;5(5):1302–1315. PubMed PMID: 24290752; PubMed Central PMCID: PMC3957429.

[100] Ishibashi S, Yamazaki T, Okamoto K. Association of autophagy with cholesterol-accumulated compartments in Niemann-Pick disease type C cells. J Clin Neurosci. 2009 Jul;16(7):954–959.. PubMed PMID: 19342246

[101] Huynh KK, Gershenzon E, Grinstein S. Cholesterol accumulation by macrophages impairs phagosome maturation. J Biol Chem. 2008 Dec 19;283(51):35745–35755.. PubMed PMID: 18955491.

[102] Rocha N, Kuijl C, van der Kant R, et al. Cholesterol sensor ORP1L contacts the ER protein VAP to control Rab7-RILP-p150 Glued and late endosome positioning. J Cell Biol. 2009 Jun 29;185(7):1209–1225. PubMed PMID: 19564404; PubMed Central PMCID: PMC2712958.

[103] Hoppe G, O'Neil J, Hoff HF, et al. Accumulation of oxidized lipid-protein complexes alters phagosome maturation in retinal pigment epithelium. Cell Mol Life Sci. 2004 Jul;61(13):1664–1674. PubMed PMID: 15224189.

[104] Frost LS, Lopes VS, Bragin A, et al. The contribution of melanoregulin to microtubule-associated protein 1 light chain 3 (LC3) associated phagocytosis in retinal pigment epithelium. Mol Neurobiol. 2015 Dec;52(3):1135–1151. 10.1007/s12035-014-8920-5. PubMed PMID: 25301234

[105] Xu L, Korade Z, Rosado DA Jr. et al. Metabolism of oxysterols derived from nonenzymatic oxidation of 7-dehydrocholesterol in cells. J Lipid Res. 2013 Apr;54(4):1135–1143..PubMed PMID: 23381570; PubMed Central PMCID: PMC3605989

[106] Xu L, Liu W, Sheflin LG, et al. Novel oxysterols observed in tissues and fluids of AY9944-treated rats: a model for Smith-Lemli-Opitz syndrome. J Lipid Res. 2011 Oct;52(10):1810–1820. PubMed PMID: 21817059; PubMed Central PMCID: PMC3173002.

[107] Wassif CA, Vied D, Tsokos M, et al. Cholesterol storage defect in RSH/Smith-Lemli-Opitz syndrome fibroblasts. Mol Genet Metab. 2002 Apr;75(4):325–334. PubMed PMID: 12051964.

[108] Elrick MJ, Yu T, Chung C, et al. Impaired proteolysis underlies autophagic dysfunction in Niemann-Pick type C disease. Hum Mol Genet. 2012 Nov 15;21(22):4876–4887. PubMed PMID: 22872701; PubMed Central PMCID: PMC3607480.

[109] Cox BE, Griffin EE, Ullery JC, et al. Effects of cellular cholesterol loading on macrophage foam cell lysosome acidification. J Lipid Res. 2007 May;48(5):1012–1021. PubMed PMID: 17308299.

[110] Ying L, Matabosch X, Serra M, et al. Biochemical and physiological improvement in a mouse model of Smith-Lemli-Opitz Syndrome (SLOS) following gene transfer with AAV vectors. Mol Genet Metab Rep. 2014;1:103–113..PubMed PMID: 25024934; PubMed Central PMCID: PMC4093838

[111] Muniz-Feliciano L, Doggett TA, Zhou Z, et al. RUBCN/rubicon and EGFR regulate lysosomal degradative processes in the retinal pigment epithelium (RPE) of the eye. Autophagy. 2017;13 (12):2072–2085..PubMed PMID: 28933590; PubMed Central PMCID: PMC5788552

[112] Ferrer M, Corneo B, Davis J, et al. A multiplex high-throughput gene expression assay to simultaneously detect disease and functional markers in induced pluripotent stem cell-derived retinal pigment epithelium. Stem Cells Transl Med. 2014 Aug;3(8):911–922. PubMed PMID: 24873859; PubMed Central PMCID: PMC4116245.

[113] Miyagishima KJ, Wan Q, Corneo B, et al. In pursuit of authenticity: induced pluripotent stem cell-derived retinal pigment epithelium for clinical applications. Stem Cells Transl Med. 2016 Nov;5 (11):1562–1574. PubMed PMID: 27400791; PubMed Central PMCID: PMC5070511.

[114] Saini JS, Corneo B, Miller JD, et al. Nicotinamide ameliorates disease phenotypes in a human iPSC model of age-related macular degeneration. Cell Stem Cell. 2017 May 4;20(5):635–647 e7. PubMed PMID: 28132833; PubMed Central PMCID: PMC5419856.

[115] Pfeffer BA, Xu L, Porter NA, et al. Differential cytotoxic effects of 7-dehydrocholesterol-derived oxysterols on cultured retina-derived cells: dependence on sterol structure, cell type, and density. Exp Eye Res. 2016 Apr;145:297–316. PubMed PMID: 26854824; PubMed Central PMCID: PMC5024725.

[116] Cham BE, Knowles BR. A solvent system for delipidation of plasma or serum without protein precipitation. J Lipid Res. 1976 Mar;17(2):176–181. PubMed PMID: 818332

[117] Keller RK, Mitchell DA, Goulah CC, et al. Hepatic isoprenoid metabolism in a rat model of Smith-Lemli-Opitz Syndrome. Lipids. 2013 Mar;48(3):219–229. PubMed PMID: 23361583; PubMed Central PMCID: PMC3595616.

[118] Wassif CA, Krakowiak PA, Wright BS, et al. Residual cholesterol synthesis and simvastatin induction of cholesterol synthesis in Smith-Lemli-Opitz syndrome fibroblasts. Mol Genet Metab. 2005 Jun;85(2):96–107. PubMed PMID: 15896653.

[119] Sievers F, Wilm A, Dineen D, et al. Fast, scalable generation of high-quality protein multiple sequence alignments using Clustal Omega. Mol Syst Biol. 2011 Oct 11;7:539.. PubMed PMID: 21988835; PubMed Central PMCID: PMC3261699.

[120] Marmorstein AD, Marmorstein LY, Sakaguchi H, et al. Spectral profiling of autofluorescence associated with lipofuscin, Bruch's Membrane, and sub-RPE deposits in normal and AMD eyes. Invest Ophthalmol Vis Sci. 2002 Jul;43(7):2435–2441. PubMed PMID: 12091448

[121] Yamamoto K, Yoon KD, Ueda K, et al. A novel bisretinoid of retina is an adduct on glycerophosphoethanolamine. Invest Ophthalmol Vis Sci. 2011 Nov 25;52(12):9084–9090. PubMed PMID: 22039245; PubMed Central PMCID: PMC3231846.

[122] Baltazar GC, Guha S, Lu W, et al. Acidic nanoparticles are trafficked to lysosomes and restore an acidic lysosomal pH and degradative function to compromised ARPE-19 cells. PLoS One. 2012;7(12):e49635..PubMed PMID: 23272048; PubMed Central PMCID: PMC3525582

[123] Brandl C, Zimmermann SJ, Milenkovic VM, et al. In-depth characterisation of retinal pigment epithelium (RPE) cells derived from human induced pluripotent stem cells (hiPSC). Neuromolecular Med. 2014 Sep;16(3):551–564. PubMed PMID: 24801942; PubMed Central PMCID: PMC4119585.